Tunnelling and Underground Space Technology 157 (2025) 106328

Contents lists available at ScienceDirect

Tunnelling and Underground Space Technology

journal homepage: www.elsevier.com/locate/tust

Refined hybrid structural analysis shows plastic flexibility enhancement in NATM tunnel shell

Raphael Scharf [a], Markus Brandtner [b], Bernd Moritz [c], Bernhard Pichler [a], Christian Hellmich [a,*]

[a] Institute for Mechanics of Materials and Structures, TU Wien – Technische Universität Wien, Karlsplatz 13/202, 1040 Vienna, Austria
[b] IGT Geotechnik und Tunnelbau ZT GmbH, Mauracherstraße 9, 5020 Salzburg, Austria
[c] ÖBB - Infrastruktur AG, Streckenmanagement und Anlagenentwicklung, Fachbereich Bautechnik - Tunnelbau, Europaplatz 12/1, 8020 Graz, Austria

ARTICLE INFO

Keywords:
Analytical mechanics
New Austrian Tunneling Method
Aging viscoelasticity
Plastic hinges
Shotcrete
Measurement data

ABSTRACT

State-of-the-art monitoring equipment has been a key element of the New Austrian Tunneling Method (NATM) ever since its establishment and description in the 1960s. In particular so-called hybrid methods combining geodetic displacement measurements with material and structural mechanics modeling have provided access to the ground pressure distributions acting on the shotcrete tunnel shell and its utilization degree. Herein, we explore the effect of refined observation by five (instead of the classical three) geodetic laser reflectors positioned at so-called measurement points, as installed with the top heading of the tunnel Stein realized by the Austrian federal railways (ÖBB) in the south of Austria: An analytical model for the equilibrium and the deformations of aging viscoelastic cylindrical shells is specified for the displacements recorded at the measurement points, and utilization is assessed in terms of (plastic) moment-force interactions. The corresponding results widen the perception of the fundamental load-carrying characteristics of the NATM: Rather than monolithically, the tunnel shell, due to the formation of plastic hinges, may act as a literally flexible mechanical system, well adapting to the heterogeneous behavior of the surrounding ground.

1. Introduction

The New Austrian Tunneling Method (NATM), as introduced to the engineering community in the 1960s by L. v. Rabcewicz (Rabcewicz, 1964a,b, 1965), is characterized by carefully monitoring the shotcrete tunnel shell, originally by convergence measurements (Fenner, 1938; Pacher, 1964), and since the 1990s, by 3D geodetic, laser-optical displacement measurements (Schubert et al., 2002; Steindorfer et al., 1995). The latter are customarily used to foresee changes in the rock mass lying ahead of the tunnel face (Schubert and Steindorfer, 1996); and they can also be used for validation of large scale Finite Element simulations of the demanding sequence of construction steps encountered with the NATM (Gamnitzer et al., 2023). Such numerical simulations are also useful to guide, together with artificial intelligence approaches such as reinforced learning, the NATM tunnel design stage (Soranzo et al., 2022).

At the same time, it has turned out as particularly useful to combine the aforementioned laser-optical displacement measurements with structural and material mechanics representations of the hydrating tunnel shell, so as to examine the latter in terms of load carrying behavior and safety. This strategy has been coined as "hybrid method" (Hellmich et al., 1999a, 2001, 2020), and it has been refined over the last quarter of a century. At first, this concerned the choice of the mathematical functions used for the interpolation of displacements between the measurement points (Brandtner et al., 2007; Ullah et al., 2010), so as to arrive at displacement fields entering a subsequent mechanical analysis. The latter comprises the following steps: The displacement fields are first transformed into strain fields, which then enter an appropriate material model for shotcrete. The latter considers hydration-dependent, i.e. aging elastic, creep, and strength properties (Ullah et al., 2012; Hellmich and Mang, 2005), and delivers corresponding stress fields, which give access to the safety level of the shell, in terms of utilization degrees. Recently, the mathematical structure of the displacement fields between the measurement points has been directly inferred from the equilibrium conditions for cylindrical tunnel shells (Scharf et al., 2022, 2024), whereby the latter were derived from the principle of virtual power (Germain, 1973a,b; Touratier, 1992; Höller et al., 2019). The latter approach has also provided access to the ground pressure acting from the surrounding ground onto the shotcrete tunnel shell. This has led to an improvement of earlier ground pressure estimates (Ullah et al., 2013), which had been based on postprocessing stresses arising from *ad hoc* interpolation of displacement data stemming from geodetic measurements. Over the same 25 years, also the geodetic monitoring

* Corresponding author.
E-mail address: Christian.Hellmich@tuwien.ac.at (C. Hellmich).

https://doi.org/10.1016/j.tust.2024.106328
Received 2 August 2024; Received in revised form 17 November 2024; Accepted 9 December 2024
Available online 27 December 2024

Nomenclature

List of Symbols

A_i	piecewisely linear shape functions (with $i = 1, \dots, 8$)
$a_{s,i}, a_{s,o}$	Cross-sectional area of the inner and the outer, circumferentially oriented reinforcement per unit length in tunnel driving direction
$\mathbf{e}_r, \mathbf{e}_\varphi, \mathbf{e}_z$	unit base vectors of (cylindrical) coordinate system, moving along an arc
$\mathbf{e}_x, \mathbf{e}_y, \mathbf{e}_z$	unit base vectors of Cartesian coordinate system, fixed in space
E	elastic modulus (Young's modulus) of shotcrete
$E_{28\mathrm{d}}$	28-day value of E
E_c	creep modulus of shotcrete
$E_{c,28\mathrm{d}}$	28-day value of E_c
E_s	elastic modulus of steel reinforcement
f_b	biaxial compressive strength of shotcrete
f_c	uniaxial compressive strength of shotcrete
f_c^*	reference strength level
$f_{c,28\mathrm{d}}$	28-day value of f_c
$\mathbf{G}_p$	ground pressure vector field
G_p	ground pressure
$G_{p,i}$	ground pressure at position i (with $i = 1, \dots, 8$)
H	Heaviside function
h	thickness of tunnel shell segment
J	creep function
J_d	creep rate function
k	index numbering plastic hinges
m	index numbering time steps
m_z	bending moment around an axis in $\mathbf{e}_z$-direction and positioned on the midsurface of the tunnel shell segment (per length measured in tunnel driving direction e_z)
m_z^p	plastic bending moment
$\mathbf{N}_p$	external circumferential force vector
N_p	impost force (per length measured in tunnel driving direction e_z)
N_t	number of time steps
N_k	number of plastic hinges
n	index numbering time steps
$\mathbf{n}$	outward normal onto a surface element
n_φ	circumferential normal force (per length measured in tunnel driving direction e_z)
n_R^*, m_R^*	circumferential normal force and bending resistances of an $\mathbf{e}_r(\varphi)$-oriented shell segment generator
$n_{R,i}, m_{R,i}$	circumferential normal force and bending resistances of the vertices of the polygonal failure surface in the force-over-bending-moment plane (with i running from A to P)
p_i, q_i	fitting parameter for the fitting function of the displacement measurements
R	radius of the undeformed midsurface of a tunnel shell segment
R_i	radius of the inner surface of the tunnel shell segment
r	radial coordinate
r_c	distance of the gravitational center of the concrete compression zone from the shell midsurface
$r_{s,i}, r_{s,o}$	distance of the inner and the outer reinforcement from the shell midsurface
s_E	dimensionless parameter quantifying strength and elastic modulus evolution
s_{E_c}	dimensionless parameter quantifying creep modulus evolution
t	time variable associated with recording of strain or displacement values
t_0^*	reference time
u_{fit}	fitting function for the corresponding displacement trends
u_r^M, u_φ^M	radial and circumferential displacements at the midsurface of the cylindrical tunnel shell segments
$u_r^{\mathrm{MP}i}, u_\varphi^{\mathrm{MP}i}$	polar displacements recorded at measurement point i (with $i = 1, 2, 3, 4, 5$)
$u_{r,fit}^{\mathrm{MP}i}, u_{\varphi,fit}^{\mathrm{MP}i}$	polar displacements fitted at measurement point i (with $i = 1, 2, 3, 4, 5$)
$u_{r,RI}^M, u_{\varphi,RI}^M$	radial and circumferential displacements of the midsurface at the right impost of the arch-like tunnel cross section
$\mathbf{x}$	position vector
x_B	height of the concrete compression zone
z	axial coordinate, associated with tunnel driving direction
α	dimensionless parameter related to the shotcrete aggregates
β	creep-related power-law exponent
δ	Dirac function
$\Delta\varphi$	central angle of circular tunnel shell arc
Δt_n	time increment
ε	small positive number
ε_{cu2}	maximum compressive strain of shotcrete
ε_{c2}	compressive strain of shotcrete at the (compressive) strength limit
ε_{sy}	yield strain of the reinforcement
η	affine creep magnification factor
θ_z^M	rotational angle of the shell generator line, around an axis oriented in $\mathbf{e}_z$-direction and positioned on the midsurface of the tunnel shell segment
$\theta_{z,LI}^M, \theta_{z,RI}^M$	rotational angle of the shell generator line, around an axis oriented in $\mathbf{e}_z$-direction and positioned on the midsurface at the left and the right impost of the arch-like tunnel cross section, respectively
$[\![\theta_z^M]\!]_k$	jump in generator rotation at the kth plastic hinge
κ	ratio of biaxial to uniaxial compressive strength of shotcrete

ν	Poisson's ratio
ξ	hydration degree of shotcrete
$\sigma_{s,i}, \sigma_{s,o}$	stress of the inner and the outer reinforcement
τ	time instant of load application
φ	azimuthal coordinate
$\varphi^{\mathrm{MP}i}$	azimuthal coordinate of the measurement points MPi, with $i = 1, 2, 3, 4, 5$
$\varphi_{LI}, \varphi_{RI}$	azimuth of the left and the right impost of the arch-like tunnel cross section, respectively
$\bar{\varphi}$	inclined azimuthal coordinate, measured from the right impost of the arch-like tunnel cross section
$\bar{\varphi}_k$	inclined azimuthal coordinate of the kth plastic hinge
$\bar{\varphi}_i$	inclined azimuthal coordinate of the ground pressure intensity $G_{p,i}$, with $i = 1, \ldots, 8$
$\mathcal{I}_{i\to r}$	azimuth-dependent influence function related to the effect of (external) ground pressure at position i, on radial displacement distribution (with $i = 1, \ldots, 8$)
$\mathcal{I}_{i\to\varphi}$	azimuth-dependent influence function related to the effect of (external) ground pressure at position i, on circumferential displacement distribution (with $i = 1, \ldots, 8$)
$\mathcal{I}_{i\to z}$	azimuth-dependent influence function related to the effect of (external) ground pressure at position i, on rotational angle distribution (with $i = 1, \ldots, 8$)
$\mathcal{I}_{i\to f}$	azimuth-dependent influence function related to the effect of (external) ground pressure at position i, on (internal) circumferential force distributions (with $i = 1, \ldots, 8$)
$\mathcal{I}_{N\to r}$	azimuth-dependent influence function related to the effect of right and left (external) impost forces, on radial displacement distribution
$\mathcal{I}_{N\to\varphi}$	azimuth-dependent influence function related to the effect of right and left (external) impost forces, on circumferential displacement distribution
$\mathcal{I}_{N\to z}$	azimuth-dependent influence function related to the effect of right and left (external) impost forces, on rotational angle distribution
$\mathcal{I}_{N\to f}$	azimuth-dependent influence function related to the effect of right and left (external) impost forces, on (internal) circumferential force distributions
$\mathcal{I}_{z,k\to r}$	azimuth-dependent influence function related to the effect of plastic rotational angle, on radial displacement distribution
$\mathcal{I}_{z,k\to\varphi}$	azimuth-dependent influence function related to the effect of plastic rotational angle, on circumferential displacement distribution
$\mathcal{U}$	generator-specific utilization degree
$\mathcal{U}_{glob}$	degree of utilization at structure level, i.e. at the level of the entire measuring cross-section

arrangements themselves have been refined: Early benchmark examples like the Sieberg tunnel (Ramspacher and Druckfeuchter, 1999), on which several of the aforementioned variants of the hybrid method have been developed, were equipped with three measurement points in the top heading of the tunnel shell, while more recent structures, such as the newly built tunnels in the network of the Austrian federal railways (Schubert and Moritz, 2011), or the Laliki tunnel in the south of Poland (Niedbalski et al., 2018), were equipped with five measurement points.

This motivates an obvious, but still fundamental, research question: Does the availability of additional measurement data enrich, or even alter, the mechanical understanding of the monitored tunnel structure?

The present paper wishes to provide a first answer to this question, along the following lines: The scene is set, in Section 2, by describing the NATM-driven portion of tunnel Stein realized by the Austrian federal railways (ÖBB) in the south of Austria (Benedikt et al., 2016). This tunnel crosses Miocene sediments alternating with cemented conglomerate and consolidated soils. Thereby, our focus is on the geometrical and material properties of the top heading of cross section KMA5.3.000201, together with its geodetic equipment, including five reflectors functioning as laser-optical 3D displacement measurement points, and with corresponding data collected over a time span of about 300 days. This top heading is represented by means of an analytical structural mechanics model of the tunnel shell with aging viscoelastic properties of the shotcrete, described in Section 3. In this context, particular emphasis is put on the extension of the analytical expressions which have been presented by Scharf et al. (2022, 2024), to the situation where plastic hinges may form in the shotcrete tunnel. Such hinges lead to a further enhancement of the "flexibility" of the tunnel shell — one of the hallmarks of the NATM (Karakuş and Fowell, 2004). The conditions under which such hinges may form are described thereafter, in Section 4. All these model ingredients finally allow for conversion of displacement measurement data into spatial and temporal distributions of ground pressures, axial forces, bending moments, stresses, and degrees of utilization, as reported in Section 5. Corresponding results are reported thereafter, in Section 6, before the paper is concluded in Section 7.

2. Characteristics of tunnel Stein: construction methods, geometry, material, geology, monitoring equipment and data

2.1. Construction methods, geometrical and material properties

Tunnel Stein is part of the new Koralmbahn railway connecting the Austrian cities Graz and Klagenfurt, along the Baltic-Adriatic corridor. This tunnel has a total length of 2100 m, a maximum overburden of 31 m, and it was built according to two different construction methods: Starting from the east portal, cut-and-cover construction was used for 565 m, while the majority of the tunnel length, the remaining 1535 m, were driven according to the NATM, see Fig. 1. The geometrical properties of a typical cross section of the NATM-driven portion of tunnel Stein, namely cross section KMA5.3.000201, are illustrated in Fig. 3. Furthermore, we consider a (mean) shell thickness of $h = 0.30$ m, and a typical shotcrete mixture, based on cement type CEM II/A-S 42.5R and with strength class SpC 20/25. Moreover, we consider peripherally placed AQ60 reinforcement meshes and a centrally positioned P95/20/30 lattice girder, with all these reinforcing elements being made from steel BSt 550.

As concerns the NATM-portion of tunnel Stein, the driving process took place from both portals, in the following way: The top heading with a temporary invert was advanced first, at a rate of 3.25 m/d, followed by a coupled bench/invert advance with about 6.00 m/d, see Fig. 2. In more detail, the following construction steps were realized (see also Fig. 4 for construction photos):

- Step #1: Excavation and installation of the top heading including its feet
- Step #2: Installation of the temporary invert arch and of the first rock bolts
- Step #3: Demolition of the temporary top heading invert arch and excavation of the benches
- Step #4: Installation of the shell portions at the benches, and of additional rock bolts

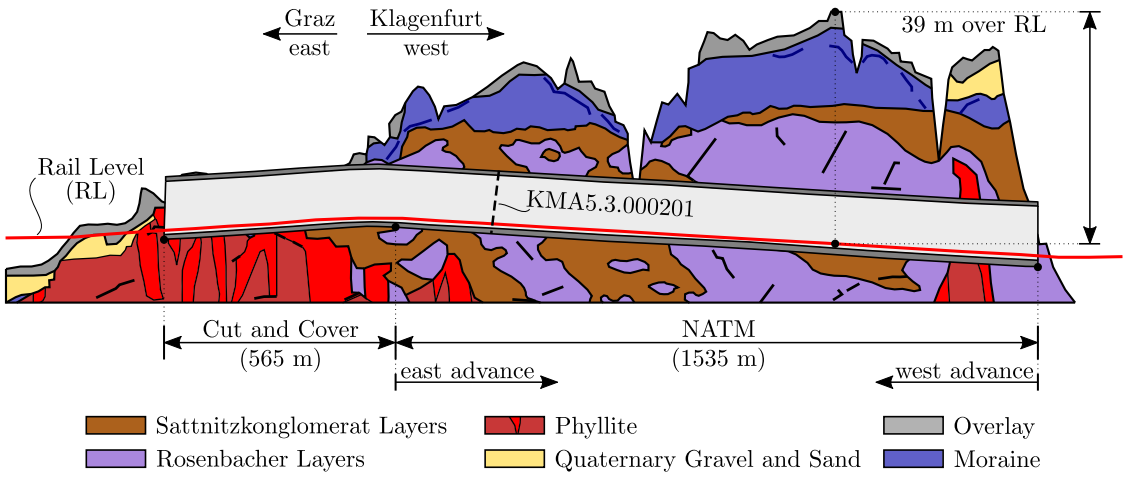

Fig. 1. Geological longitudinal section of tunnel Stein, with indication of the different construction methods used, and of measurement cross-section KMA5.3.000201, investigated herein; drawn after (Benedikt et al., 2016).

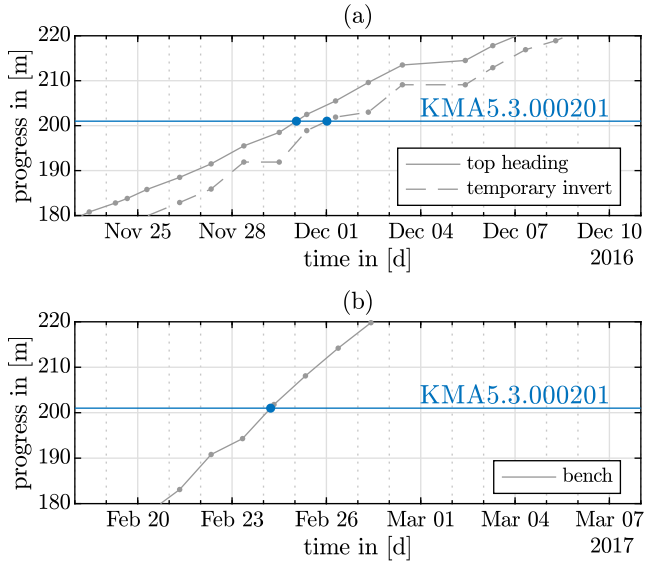

Fig. 2. Construction progress of tunnel Stein: (a) top heading and temporary invert, (b) bench (the invert is installed one day later).

- Step #5: Excavation and installation of the invert arch

According to Fig. 2, Step #3 was realized some 80 to 90 days after Step #2.

2.2. Geological conditions

Tunnel Stein is located in the eastern part of the inter-alpine basin called Klagenfurter Becken, which consists of the Palaeozoic basement of the Magdalensberg series (quartz phyllite) and overlying moraines. From a geological point of view, essentially two layers are found in the NATM-driven portion of tunnel Stein (Benedikt et al., 2016): (i) the Sattnitz conglomerate layers, consisting of densely consolidated soils or cemented conglomerate, and (ii) the Rosenbacher layers, made of fine-grained Miocene sediments with local coal seams, see Fig. 1.

2.3. Displacement data at five measurement points, and temporal fitting

We here focus on cross section KMA5.3.000201, located 201 m west of the eastern end of the NATM-driven portion of tunnel Stein, and

Table 1
Initial geodetic positions of the measurement points attached to the top heading of measurement cross section KMA5.3.000201, recorded at November 30, 2016 at 9 a.m.

Measurement point	H	V	L
KMA5.3.000201.1	+1.151 m	+8.566 m	+201.497 m
KMA5.3.000201.2	−2.598 m	+6.333 m	+200.626 m
KMA5.3.000201.3	+7.135 m	+6.472 m	+200.519 m
KMA5.3.000201.4	−3.676 m	+4.378 m	+200.644 m
KMA5.3.000201.5	+8.389 m	+4.466 m	+200.612 m

equipped with five reflectors, which are positioned at measurement points MP1 to MP5, see Figs. 3 and 4 for blueprint and photo illustrations, respectively. Displacements of these measurement points are defined with respect to their geodetic positions recorded on November 30, 2016, at 9 a.m., see Table 1.

These positions also allow for reconstruction of the actual shell geometry in terms of the following quantities: the inner radius of the arc amounts to $R_i = 6.40$ m, the opening angle of the top heading of the considered cross section spans $\Delta\varphi = 174.40°$ from one foot to the other, as also seen in Fig. 7; and the positions of the five measurement points, in terms of the polar angle given in Fig. 7, amount to $\varphi^{MP5} = 19.95°$, $\varphi^{MP3} = 41.33°$, $\varphi^{MP1} = 101°$, $\varphi^{MP2} = 140.77°$, and $\varphi^{MP4} = 160.89°$. The positions of the right and left impost, respectively, are quantified through $\varphi_{RI} = 2.8°$ and $\varphi_{LI} = 177.2°$; $\varphi_{LI} - \varphi_{RI} = \Delta\varphi$.

After the initial recording, positions are measured on a daily basis, and subtracting the initial position from the current position yields the displacement vectors at the measurement points, see Fig. 5 as well as Tables 7 and 8. The corresponding displacement trends are represented by two types of fitting functions that allow for suitable representation of the data, see also Table 2: The first type is used from the first measurement up to immediately before the excavation of the bench, and it reads as

$$u_{fit}(t) = \frac{p_1\, t^2 + p_2\, t}{t + p_3}\,, \quad \text{for } 0 \le t \le 84.96\,\text{d}\,, \tag{1}$$

with the fitting parameters p_1, p_2, and p_3 according to Table 3. The second type of fitting function is used for displacements recorded from the bench excavation onwards, and it reads as

$$u_{fit}(t) = \frac{q_1\,(t-q_5)^2 + q_2\,(t-q_5)}{(t-q_5)^2 + q_3\,(t-q_5) + q_4}\,, \quad \text{for } t > 84.96\,\text{d}\,, \tag{2}$$

with the fitting parameters q_1, q_2, q_3, q_4, and q_5 according to Table 3.

3. Analytical structural mechanics model of shotcrete tunnel shell

A recently developed analytical structural mechanics model for top headings of aging viscoelastic cylindrical tunnel shells under plane

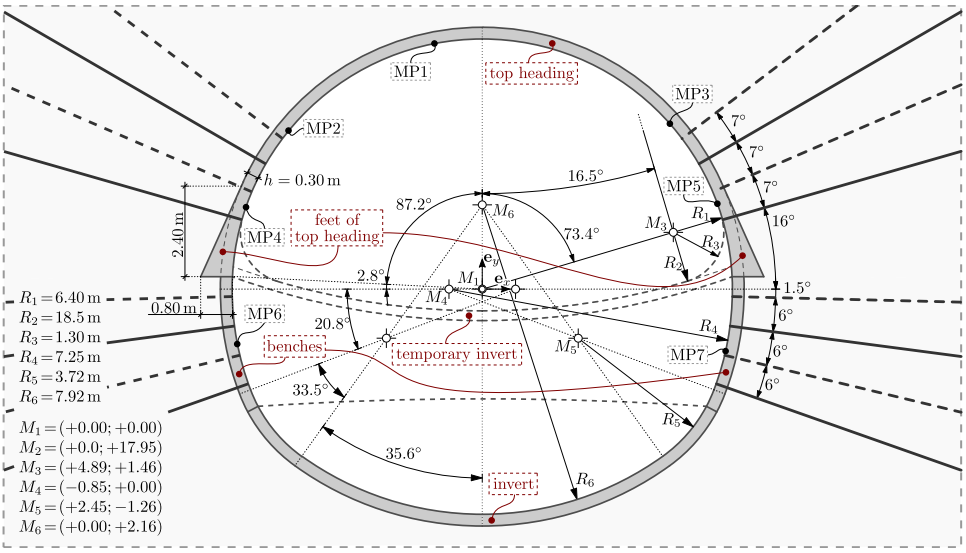

Fig. 3. Measurement cross-section KMA5.3.000201, after completed construction: illustration of the components of the shotcrete shell and of the rock bolts; indication of arc centers, of arc radii, of arc angles, and of measurement points MP1 to MP7.

Fig. 4. Construction and monitoring photos of tunnel Stein: (a) top heading and temporary invert installed, (b) installation of top heading only, and (c) excavation of the benches; with labeling of tunnel shell portions, rock bolts, reinforcement elements, and measurement point locations, photographs (a) and (b) by courtesy of ÖBB-Infrastruktur AG; photograph (c) reproduced from Figure 6 of (Herzeg and Moraus, 2017), with permission of John Wiley and Sons.

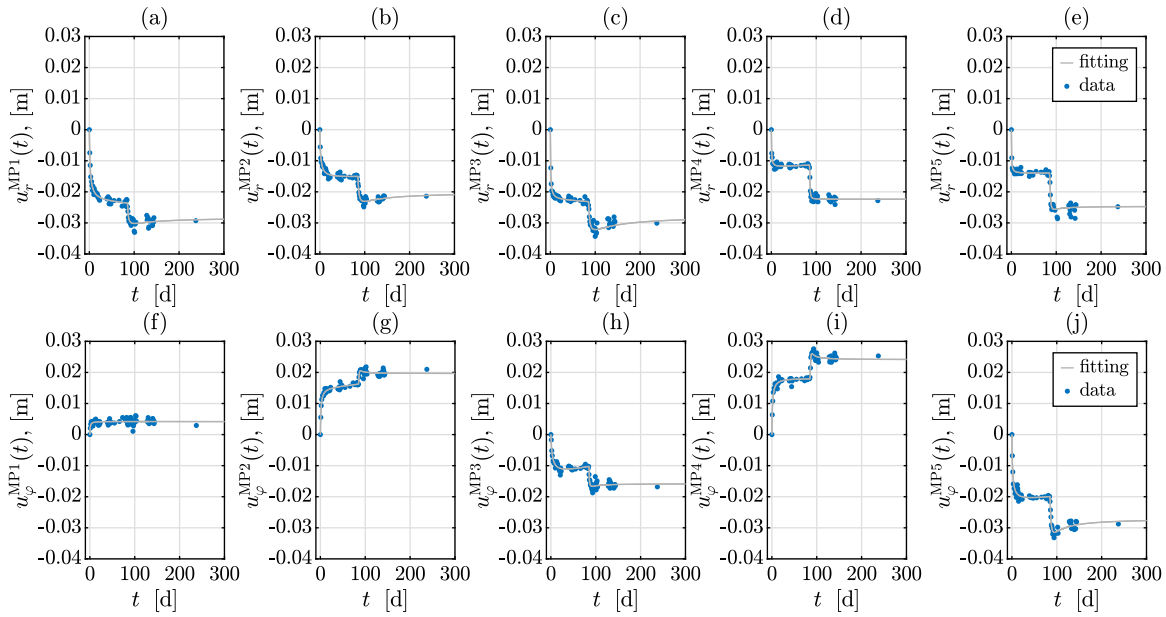

Fig. 5. Illustration of the displacement measurements at MP1 to MP5 of cross section KMA5.3.000201, in terms of the evolutions of the radial components (a-e) and of the circumferential components (f-j); together with fitting functions according to Eqs. (1) and (2).

Table 2
Goodness-of-Fit Statistics for the fitting functions to describe the radial and tangential displacement measurements at MP1 to MP5: R-Square and Root Mean Square Error.

	$u_{r,fit}^{MP1}$	$u_{r,fit}^{MP2}$	$u_{r,fit}^{MP3}$	$u_{r,fit}^{MP4}$	$u_{r,fit}^{MP5}$
R-Square [-]	0.9642	0.9568	0.9639	0.9502	0.9273
RMSE [m]	9.7×10^{-4}	7.3×10^{-4}	9.4×10^{-4}	6.5×10^{-4}	1.1×10^{-3}
	$u_{\varphi,fit}^{MP1}$	$u_{\varphi,fit}^{MP2}$	$u_{\varphi,fit}^{MP3}$	$u_{\varphi,fit}^{MP4}$	$u_{\varphi,fit}^{MP5}$
R-Square [-]	0.9260	0.9547	0.8960	0.9542	0.9583
RMSE [m]	8.2×10^{-4}	7.2×10^{-4}	9.1×10^{-4}	8.5×10^{-4}	9.9×10^{-4}

Table 3
Fitting parameters p_i and q_i for the functional description of the radial and tangential displacement evolution.

Parameters	$u_{r,fit}^{MP1}$	$u_{r,fit}^{MP2}$	$u_{r,fit}^{MP3}$	$u_{r,fit}^{MP4}$	$u_{r,fit}^{MP5}$
p_1 [m/d]	−1.06e-5	+5.53e-6	−8.35e-6	+9.02e-6	+1.12e-6
p_2 [m]	−0.0232	−0.0158	−0.0226	−0.0122	−0.0141
p_3 [d]	+1.8300	+1.8200	+0.6433	+0.5330	+0.4033
q_1 [m]	−0.0283	−0.0201	−0.0278	−0.0224	−0.0246
q_2 [md]	−1.3000	−0.9652	−0.7708	+0.0089	−0.0441
q_3 [d]	+40.980	+37.930	+21.460	−0.3635	+0.8286
q_4 [d^2]	+17.480	+30.130	+17.850	+0.5578	+5.2010
q_5 [d]	+84.000	+84.000	+84.000	+84.000	+84.000
parameters	$u_{\varphi,fit}^{MP1}$	$u_{\varphi,fit}^{MP2}$	$u_{\varphi,fit}^{MP3}$	$u_{\varphi,fit}^{MP4}$	$u_{\varphi,fit}^{MP5}$
p_1 [m/d]	−1.86e-7	+1.43e-5	+2.93e-5	−2.71e-6	+1.64e-5
p_2 [m]	+0.0042	+0.0153	−0.0131	+0.0184	−0.0217
p_3 [d]	+0.6977	+1.2830	+3.1730	+1.3840	+1.4950
q_1 [m]	–	+0.0197	−0.0158	+0.0241	−0.0270
q_2 [md]	–	+4.88e-05	−0.0971	−0.0029	−0.5385
q_3 [d]	–	−0.4356	+5.0250	−0.8723	+14.030
q_4 [d^2]	–	+1.1210	+3.3150	+1.9330	+16.790
q_5 [d]	–	+84.000	+84.000	+84.000	+84.000

strain conditions (Scharf et al., 2022, 2024) provides closed-form solutions for circumferential normal forces per unit length, n_φ, for bending moments per unit length around the tunnel axis direction, m_z, and for kinematic descriptors of the shell midsurface, namely circumferential displacements u_φ^M, radial displacements u_r^M, and generator rotations θ_z^M around the tunnel axis direction; always as functions of the ground pressure distributions $G_p(\varphi)$ and the impost forces N_p. When (fictitiously) cutting free the interfaces between top heading and ground, which, at the imposts, become interfaces between top heading and bench after installation of the latter, the corresponding "new" surfaces with unit normal vectors $\mathbf{n}=\mathbf{e}_r(\varphi)$, $\varphi_{RI}\le\varphi\le\varphi_{LI}$, $\mathbf{n}=-\mathbf{e}_\varphi(\varphi_{RI})$, and $\mathbf{n}=\mathbf{e}_\varphi(\varphi_{LI})$ are subjected to (external) traction forces, see Fig. 6. The outer surface of the shell, with normal $\mathbf{n}=\mathbf{e}_r(\varphi)$, is subjected to the ground pressure vector field, which mathematically reads as

$$\mathbf{G}_p\big(\mathbf{x}=(R+h/2)\,\mathbf{e}_r(\varphi),\mathbf{n}=\mathbf{e}_r(\varphi)\big)=-G_p(\varphi)\,\mathbf{e}_r(\varphi)\,, \tag{3}$$

with G_p being positive for a pressure acting onto the tunnel shell segment. External traction forces also act on the surfaces at the beginning and the end of circular shell segment, with normal vectors $\mathbf{n}=-\mathbf{e}_\varphi(\varphi_{RI})$ and $\mathbf{n}=\mathbf{e}_\varphi(\varphi_{LI})$. Integrating the latter over the shell thickness yields external circumferential force vectors, the orientations of which depend on the orientation of the surface on which they act; mathematically, this reads as

$$\mathbf{N}_p\big(\mathbf{x}=R\,\mathbf{e}_r(\varphi_{RI}),\mathbf{n}=-\mathbf{e}_\varphi(\varphi_{RI})\big)=N_p\,\mathbf{e}_\varphi(\varphi_{RI})\,, \tag{4}$$

$$\mathbf{N}_p\big(\mathbf{x}=R\,\mathbf{e}_r(\varphi_{LI}),\mathbf{n}=\mathbf{e}_\varphi(\varphi_{LI})\big)=-N_p\,\mathbf{e}_\varphi(\varphi_{LI})\,. \tag{5}$$

For the present application, we consider a piecewisely linear distribution of the ground pressure, according to

$$G_p(\bar\varphi)=\sum_{i=1}^{8}A_i(\bar\varphi)\,G_{p,i}\,, \tag{6}$$

where $G_{p,i}$ is the ground pressure at position $\bar\varphi=\bar\varphi_i$, with the variable $\bar\varphi$ being measured from the right impost, $\bar\varphi=\varphi-\varphi_{RI}$, see Fig. 7. This piecewisely linear distribution is defined through values associated with the positions $\bar\varphi_1=0°$, $\bar\varphi_2=24.91°$, $\bar\varphi_3=49.83°$, $\bar\varphi_4=74.74°$, $\bar\varphi_5=99.66°$, $\bar\varphi_6=124.57°$, $\bar\varphi_7=149.49°$, and $\bar\varphi_8=174.40°$, with kinks at positions $\bar\varphi_2$ through $\bar\varphi_7$. The corresponding piecewisely linear shape functions A_i, with $i=1,2,\dots,8$ read as

$$A_1(\bar\varphi)=1-\frac{\bar\varphi-\bar\varphi_1}{\bar\varphi_2-\bar\varphi_1}\,H(\bar\varphi-\bar\varphi_1)+\frac{\bar\varphi-\bar\varphi_2}{\bar\varphi_2-\bar\varphi_1}\,H(\bar\varphi-\bar\varphi_2)\,, \tag{7}$$

$$\begin{aligned}A_i(\bar\varphi)=&\frac{\bar\varphi-\bar\varphi_{i-1}}{\bar\varphi_i-\bar\varphi_{i-1}}\,H(\bar\varphi-\bar\varphi_{i-1})-\frac{\bar\varphi-\bar\varphi_i}{\bar\varphi_i-\bar\varphi_{i-1}}\,H(\bar\varphi-\bar\varphi_i)\\&-\frac{\bar\varphi-\bar\varphi_i}{\bar\varphi_{i+1}-\bar\varphi_i}\,H(\bar\varphi-\bar\varphi_i)+\frac{\bar\varphi-\bar\varphi_{i+1}}{\bar\varphi_{i+1}-\bar\varphi_i}\,H(\bar\varphi-\bar\varphi_{i+1})\,,\end{aligned} \tag{8}$$

with $i=2,\dots,7$, and as

$$A_8(\bar\varphi)=\frac{\bar\varphi-\bar\varphi_7}{\bar\varphi_8-\bar\varphi_7}\,H(\bar\varphi-\bar\varphi_7)\,, \tag{9}$$

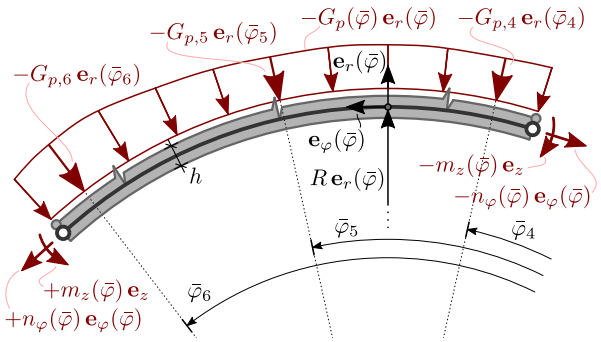

Fig. 6. External forces resulting from (fictitiously) cutting free a portion of the tunnel shell: traction forces associated with ground pressure, circumferential forces, and bending moments.

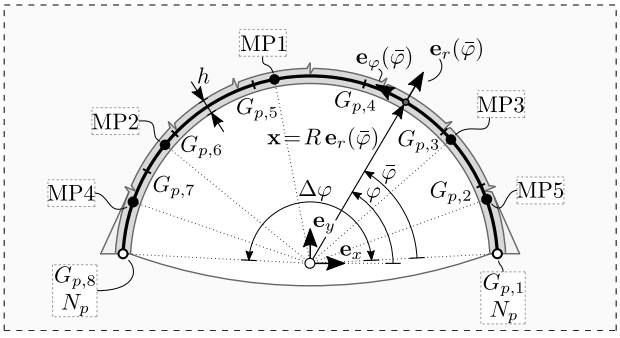

Fig. 7. Structural model of the measurement cross-section KMA5.3.000201: Illustration of a Cartesian coordinate system with the origin in the circle center and an orthonormal base frame $\mathbf{e}_x$-$\mathbf{e}_y$, of global and local azimuthal coordinate φ and $\bar\varphi$, of location-dependent polar base frames $\mathbf{e}_r(\bar\varphi)$-$\mathbf{e}_\varphi(\bar\varphi)$, of position vector $\mathbf{x}$, of thickness h, of the positions of the measurement points MPi, with $i=1,\dots,5$, of unknown ground pressure intensities $G_{p,i}$, with $i=1,\dots,8$, and of unknown impost force N_p.

whereby H denotes the Heaviside-function, see also Fig. 8. The corresponding distribution of circumferential normal forces along the shell segment reads as

$$n_\varphi(\bar\varphi) = N_p\,\mathcal{I}_{N\to f}(\bar\varphi) + \sum_{i=1}^{8} R\,G_{p,i}\,\mathcal{I}_{i\to f}(\bar\varphi)\,, \tag{10}$$

with R as the radius of the cylindrical shell segment, see Fig. 7, and with the (external)-traction-to-(internal)-force influence functions $I_{N\to f}$, and $I_{i\to f}$, concerning the influence of the right and left (external) impost forces, and of the (external) ground pressure values at the positions $\bar\varphi_1$ through $\bar\varphi_8$, on the (internal) circumferential forces. The corresponding mathematical relations are given in the Appendix, as Eqs. (57) and (58). These influence functions also allow for the quantification of the bending moments arising from impost force and ground pressure values, namely in the format

$$m_z(\bar\varphi) = R\,N_p\big[1-\mathcal{I}_{N\to f}(\bar\varphi)\big] + \sum_{i=1}^{8} R^2\,G_{p,i}\,\mathcal{I}_{i\to f}(\bar\varphi)\,, \tag{11}$$

and we note in passing that these bending moments need to fulfill the following natural boundary conditions (Scharf et al., 2022),

$$\text{for } \bar\varphi=0 \text{ and } \bar\varphi=\Delta\varphi\,,\qquad \frac{1}{R}\frac{\mathrm{d}m_z(\bar\varphi)}{\mathrm{d}\varphi}=0\,. \tag{12}$$

As regards radial and circumferential displacements at the midsurface of the tunnel shell segment, u_r^M and u_φ^M, as well as the rotational angle of the shell generator lying perpendicular to the midsurface of the tunnel shell segment, denoted as θ_z^M, the expressions given in (Scharf et al., 2024) are now complemented by discontinuities in the generator rotations arising from plastic bending moments developing at azimuthal positions $\bar\varphi_k$. These discontinuities, indicating so-called "plastic hinges", are denoted as $[\![\theta_z^M]\!]_k$. Accordingly, the kinematic evolution of the tunnel shell, when given as function of the rates of impost forces and ground pressure values, reads as

$$\begin{aligned}
&+\dot u_r^M(\bar\varphi,t) - \dot u_{\varphi,RI}^M(t)\sin(\bar\varphi) - \dot u_{r,RI}^M(t)\cos(\bar\varphi)\\
&+R\,\dot\theta_{z,RI}^M(t)\sin(\bar\varphi) = \sum_{k=1}^{N_k} R\,[\![\dot\theta_z^M]\!]_k(t)\mathcal{I}_{z,k\to r}(\bar\varphi)\\
&+\mathcal{I}_{N\to r}(\bar\varphi)\int_0^t J_d\big(\xi(t),\eta(t),t-\tau\big)\dot N_p(\tau)\,\mathrm{d}\tau\\
&+\sum_{i=1}^{8}\mathcal{I}_{i\to r}(\bar\varphi)\int_0^t J_d\big(\xi(t),\eta(t),t-\tau\big)\dot G_{p,i}(\tau)\,\mathrm{d}\tau,
\end{aligned} \tag{13}$$

$$\begin{aligned}
&+\dot u_\varphi^M(\bar\varphi,t) - \dot u_{\varphi,RI}^M(t)\cos(\bar\varphi) + \dot u_{r,RI}^M(t)\sin(\bar\varphi)\\
&+R\,\dot\theta_{z,RI}^M(t)\big(\cos(\bar\varphi)-1\big) = \sum_{k=1}^{N_k} R\,[\![\dot\theta_z^M]\!]_k(t)\mathcal{I}_{z,k\to\varphi}(\bar\varphi)\\
&+\mathcal{I}_{N\to\varphi}(\bar\varphi)\int_0^t J_d\big(\xi(t),\eta(t),t-\tau\big)\dot N_p(\tau)\,\mathrm{d}\tau\\
&+\sum_{i=1}^{8}\mathcal{I}_{i\to\varphi}(\bar\varphi)\int_0^t J_d\big(\xi(t),\eta(t),t-\tau\big)\dot G_{p,i}(\tau)\,\mathrm{d}\tau,
\end{aligned} \tag{14}$$

$$\begin{aligned}
&+\dot\theta_z^M(\bar\varphi,t) - \dot\theta_{z,RI}^M(t) = \sum_{k=1}^{N_k}[\![\dot\theta_z^M]\!]_k(t)\,H(\bar\varphi-\bar\varphi_k)\\
&+\mathcal{I}_{N\to z}(\bar\varphi)\int_0^t J_d\big(\xi(t),\eta(t),t-\tau\big)\dot N_p(\tau)\,\mathrm{d}\tau\\
&+\sum_{i=1}^{8}\mathcal{I}_{i\to z}(\bar\varphi)\int_0^t J_d\big(\xi(t),\eta(t),t-\tau\big)\dot G_{p,i}(\tau)\,\mathrm{d}\tau,
\end{aligned} \tag{15}$$

where $u_{r,RI}^M$, $u_{\varphi,RI}^M$, and $\theta_{z,RI}^M$ stand for displacements and shell generators at the right impost of the shell. In Eqs. (13)–(15), spatial dependencies are quantified in terms of force-to-displacement influence functions $\mathcal{I}$, reading mathematically as,

$$\begin{aligned}
\mathcal{I}_{N\to r}(\bar\varphi) = \Big\{1-\nu^2\Big\}\Big\{&\frac{12R^3}{h^3}\Big[\cos(\bar\varphi)-1\Big]\\
&+\Big[\frac{R}{2h}+\frac{6R^3}{h^3}\Big]\Big[\frac{\bar\varphi\cos(\bar\varphi)}{\tan(\Delta\varphi)}+\bar\varphi\sin(\bar\varphi)\\
&-\frac{\sin(\bar\varphi)}{\tan(\Delta\varphi)}+\frac{\sin(\bar\varphi)}{\sin(\Delta\varphi)}-\frac{\bar\varphi\cos(\bar\varphi)}{\sin(\Delta\varphi)}\Big]\Big\},
\end{aligned} \tag{16}$$

$$\begin{aligned}
\mathcal{I}_{N\to\varphi}(\bar\varphi) = \Big\{1-\nu^2\Big\}\Big\{&\Big[\frac{R}{2h}+\frac{6R^3}{h^3}\Big]\Big[+\bar\varphi\cos(\bar\varphi)\\
&-3\sin(\bar\varphi)-\frac{\bar\varphi\sin(\bar\varphi)}{\tan(\Delta\varphi)}+\frac{\bar\varphi\sin(\bar\varphi)}{\sin(\Delta\varphi)}\Big]\\
&+\frac{R}{h}\Big[+2\sin(\bar\varphi)\Big]+\frac{12R^3}{h^3}\Big[+\bar\varphi\\
&-\frac{\cos(\bar\varphi)-1}{\tan(\Delta\varphi)}+\frac{\cos(\bar\varphi)-1}{\sin(\Delta\varphi)}\Big]\Big\},
\end{aligned} \tag{17}$$

$$\begin{aligned}
\mathcal{I}_{N\to z}(\bar\varphi) = \Big\{1-\nu^2\Big\}\Big\{&\frac{12R^2}{h^3}\Big[\frac{\cos(\bar\varphi)-1}{\tan(\Delta\varphi)}\\
&+\frac{1-\cos(\bar\varphi)}{\sin(\Delta\varphi)}+\sin(\bar\varphi)-\bar\varphi\Big]\Big\},
\end{aligned} \tag{18}$$

in terms of traction-to-displacement influence functions $\mathcal{I}$, reading mathematically as,

$$\begin{aligned}
\mathcal{I}_{i\to r}(\bar\varphi) = \Big\{1-\nu^2\Big\}\Big\{&\Big[\frac{R^2}{h}+\frac{12R^4}{h^3}\Big]\Big[+\cos(\bar\varphi)\\
&+\frac{\bar\varphi\cos(\bar\varphi)}{2\tan(\Delta\varphi)}-\frac{\bar\varphi\cos(\bar\varphi)}{2\sin(\Delta\varphi)}+\frac{\bar\varphi\sin(\bar\varphi)}{2}\\
&-\frac{\sin(\bar\varphi)}{2\tan(\Delta\varphi)}+\frac{\sin(\bar\varphi)}{2\sin(\Delta\varphi)}-1\Big]\Big\}A_i(\bar\varphi)\,,
\end{aligned} \tag{19}$$

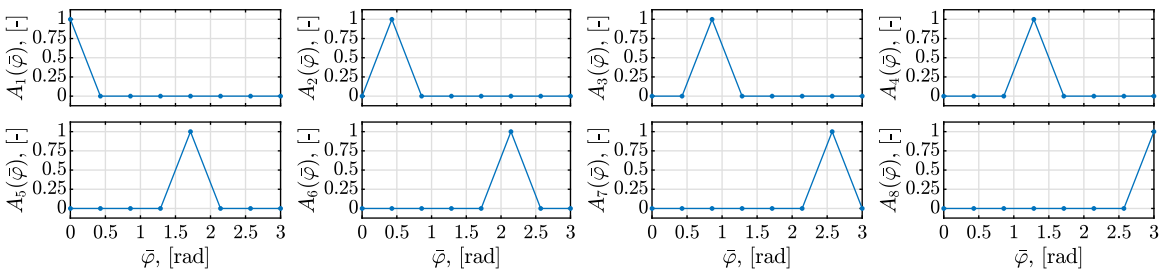

Fig. 8. Illustration of the shape functions A_i, $i = 1, \ldots, 8$, employed for the definition of the piecewisely linear ground pressure distribution according to Eq. (6).

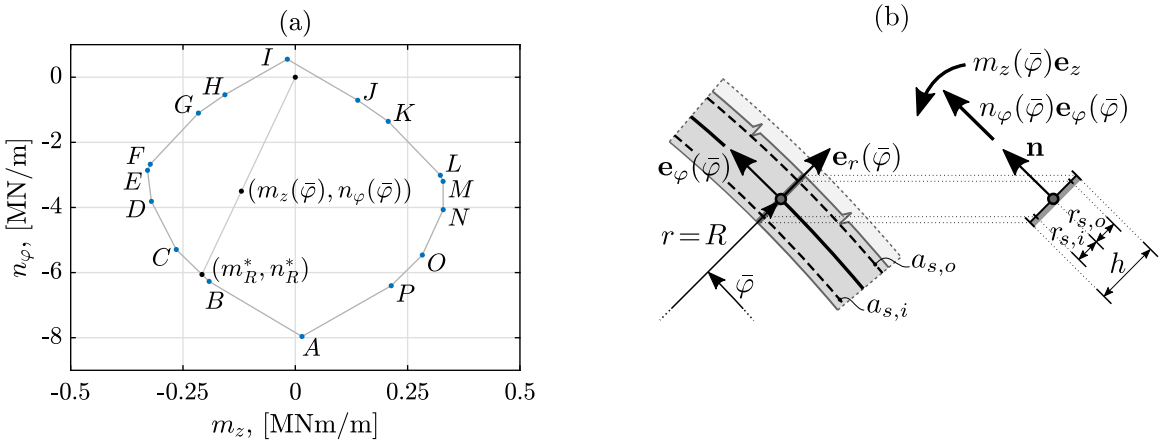

Fig. 9. Interaction diagram for normal forces and bending moments characterized by points A to P, for $f_c = 25\,\mathrm{MPa}$, $a_{s,i} = 7.55\,\mathrm{cm^2/m}$, $a_{s,o} = 4.01\,\mathrm{cm^2/m}$, $h = 0.30\,\mathrm{m}$, and $r_{s,i} = r_{s,o} = 0.105\,\mathrm{m}$ (a); and shell portion from the top heading, with forces associated with normal onto generator line (b): representation of the stress resultants $n_\varphi(\bar{\varphi})$ and $m_z(\bar{\varphi})$, the inner and outer reinforcement, and the distances to the shell midsurface $r_{s,i}$, $r_{s,o}$.

$$\begin{aligned}\mathcal{I}_{i\to\varphi}(\bar{\varphi}) = &\left\{1-\nu^2\right\}\left\{\left[\frac{R^2}{2h}+\frac{6R^4}{h^3}\right]\left[\bar{\varphi}\cos(\bar{\varphi})\right.\right.\\ &-\sin(\bar{\varphi})-\frac{\bar{\varphi}\sin(\bar{\varphi})}{\tan(\Delta\varphi)}+\frac{\bar{\varphi}\sin(\bar{\varphi})}{\sin(\Delta\varphi)}\Big]\\ &+\frac{12R^4}{h^3}\left[\bar{\varphi}+\frac{1-\cos(\bar{\varphi})}{\tan(\Delta\varphi)}\right.\\ &\left.\left.-\frac{1-\cos(\bar{\varphi})}{\sin(\Delta\varphi)}+\sin(\bar{\varphi})\right]\right\}A_i(\bar{\varphi}),\end{aligned} \tag{20}$$

$$\begin{aligned}\mathcal{I}_{i\to z}(\bar{\varphi}) = &\left\{1-\nu^2\right\}\left\{\frac{12R^3}{h^3}\left[-\bar{\varphi}+\sin(\bar{\varphi})\right.\right.\\ &\left.\left.+\frac{\cos(\bar{\varphi})-1}{\tan(\Delta\varphi)}+\frac{1-\cos(\bar{\varphi})}{\sin(\Delta\varphi)}\right]\right\}A_i(\bar{\varphi}),\end{aligned} \tag{21}$$

and in terms of plastic hinge-to-displacement influence functions $\mathcal{I}$, reading mathematically as,

$$\mathcal{I}_{z,k\to r}(\bar{\varphi}) = \left[\sin(\bar{\varphi}-\bar{\varphi}_k)\right]H(\bar{\varphi}-\bar{\varphi}_k), \tag{22}$$

$$\mathcal{I}_{z,k\to\varphi}(\bar{\varphi}) = \left[\cos(\bar{\varphi}-\bar{\varphi}_k)-1\right]H(\bar{\varphi}-\bar{\varphi}_k). \tag{23}$$

whereby $\bar{\varphi}_k$ is the azimuthal position of the k^{th} plastic hinge. Such plastic hinges occur as a result of plastic moments associated with a utilization degree of one, as described in the next section. Moreover, Eqs. (13)–(15) comprise the creep rate function of aging shotcrete, J_d (Scharf et al., 2024), which depends on the current maturity and loading state of the material, quantified by degree of hydration ξ and (internal) force-driven affinity parameter η, both evolving over time t, and on the time span $(t-\tau)$ elapsed since the time instant of load application, denoted as τ. Corresponding details are given in the next section.

4. Creep and plasticity modeling at material, generator, and cross sectional scales

Following the strategy outlined in (Scheiner and Hellmich, 2009), the creep rate function for a particular hydration and loading state of the material can be approximated by the partial derivative of a load- and hydration-dependent creep function J. When employing a power-law-type creep function, we correspondingly arrive at (Scharf et al., 2024)

$$\begin{aligned}&J_d(\xi(t),\eta(t),t-\tau) \approx \frac{\partial J}{\partial t}\left(\xi(t),\eta(t),t-\tau\right) =\\ &=\delta(t-\tau)\left\{\frac{1}{E\left(\xi(t)\right)}+\frac{\eta(t)}{E_c\left(\xi(t)\right)}\left[\frac{t-\tau}{t_0^*}\right]^\beta\right\}\\ &+H(t-\tau)\left\{\frac{\eta(t)}{E_c\left(\xi(t)\right)}\frac{\beta}{t_0^*}\left[\frac{t-\tau}{t_0^*}\right]^{\beta-1}\right\},\end{aligned} \tag{24}$$

whereby δ denotes the Dirac function, and τ stands for the time instant of load application. The power-law exponent β typically amounts to 0.25 (Ausweger et al., 2019; Königsberger et al., 2016), and the reference time t_0^* is set to 1 d, while the elastic modulus E and the creep modulus E_c can be approximated by further auxiliary functions, as described in the following.

Under isothermal conditions at 20 centigrades, the temporal evolution of the elastic modulus of shotcrete can be approximated through (Ausweger et al., 2019; CEB-FIB, 2010; Scharf et al., 2022)

$$E(t) = E_{28d}\left\{\exp\left[s_E\left(1-\sqrt{\frac{28\,\mathrm{days}}{t}}\right)\right]\right\}^{0.5}, \tag{25}$$

whereby the elastic modulus reached after 28 days amounts to

$$E_{28d} = 21.5\,\mathrm{GPa}\times\alpha\left(\frac{f_{c,28d}}{f_c^*}\right)^{0.\dot{3}}, \tag{26}$$

with the dimensionless evolution parameter s_E according to Table 4, with $f_c^* = 10\,\mathrm{MPa}$ as a reference strength level, with the uniaxial compressive strength of concrete reached 28 days after production, $f_{c,28d}$, see Table 5, with the dimensionless parameter for the stiffness of the aggregates, namely $\alpha = 1$ for quartz or limestone aggregates, and with the time t being given in the unit of measurement "days" and being resolved down to tens of minutes. As for corresponding evolutions of the degree of hydration, we refer to (Scharf et al., 2022).

Table 4
Dimensionless parameters s_E, s_{E_c} for three typical cement types (Ausweger et al., 2019).

Cement type	s_E	s_{E_c}
CEM II/A-M(S-L) 42.5N	0.22	0.62
CEM II/A-S 42.5R	0.18	0.61
CEM I 52.5R	0.09	0.50

Table 5
Uniaxial compressive strength reached 28 days after production, $f_{c,28d}$, for three typical shotcrete strength classes.

Strength Class	$f_{c,28d}$
SpC 20/25	20 MPa
SpC 25/30	25 MPa
SpC 30/37	30 MPa

Under isothermal conditions at 20 centigrades, the temporal evolution of the creep modulus of shotcrete can be approximated through (Ausweger et al., 2019; Scharf et al., 2022)

$$E_c(t) = E_{c,28d}\left\{\exp\left[s_{E_c}\left(1-\sqrt{\frac{28\,\text{days}}{t}}\right)\right]\right\}^{0.5}, \tag{27}$$

whereby the creep modulus reached after 28 days amounts to

$$E_{c,28d} = 51.9\,\text{GPa}\times\alpha^2\left(\frac{f_{c,28d}}{f_c^*}\right)^{2/3}, \tag{28}$$

with the creep modulus evolution parameter s_{E_c} according to Table 4. The affinity parameter η appearing in Eq. (24) is a fourth-order power-law function of the utilization degree $\mathcal{U}$ (Ruiz et al., 2007; Ullah et al., 2010)

$$\eta = 1 + 2\,\mathcal{U}_{glob}^4\,. \tag{29}$$

In the present case, $\mathcal{U}$ reflects the overall (internal) force state in the entire tunnel shell cross section, according to

$$\mathcal{U}_{glob}(t) = \frac{1}{\Delta\varphi}\int_{\varphi_{RI}}^{\varphi_{LI}}\mathcal{U}(\bar{\varphi},t)\,\mathrm{d}\varphi\,, \tag{30}$$

with the generator-specific utilization degree $\mathcal{U}_\varphi$. Following key standards in the field (ÖGG-Guideline, 2023; ÖNORM EN 1992-1-1, 2015), the latter depends on the generator-specific pair of circumferential normal force and bending moment around the tunnel axis, and on the ultimate load carrying capacity quantified in terms of the same two quantities. Mathematically, this reads as

$$\mathcal{U}(\bar{\varphi},t) = \frac{\left\{\left[n_\varphi(\bar{\varphi},t)\right]^2+\left[m_z(\bar{\varphi},t)\right]^2\right\}^{0.5}}{\left\{\left[n_R^*(t)\right]^2+\left[m_R^*(t)\right]^2\right\}^{0.5}}, \tag{31}$$

with n_R^* and m_R^* as the resistance values for the circumferential normal force and the bending moment around the tunnel axis. The latter are determined from a force-moment interaction diagram, and more precisely, this pair of resistance values corresponds to the intersection of the extension of the $(0,0)$-$\left(m_z(\bar{\varphi}),n_\varphi(\bar{\varphi})\right)$-line with the interaction diagram, see Fig. 9. The corresponding coordinates of the intersection point follow as

$$\begin{aligned} m_R^* &= \frac{(m_{R,j}n_{R,i}-m_{R,i}n_{R,j})\,m_z(\bar{\varphi})}{(n_{R,i}-n_{R,j})\,m_\varphi(\bar{\varphi})+(m_{R,j}-m_{R,i})\,n_\varphi(\bar{\varphi})}\,,\\ n_R^* &= \frac{(m_{R,j}n_{R,i}-m_{R,i}n_{R,j})\,n_\varphi(\bar{\varphi})}{(n_{R,i}-n_{R,j})\,m_\varphi(\bar{\varphi})+(m_{R,j}-m_{R,i})\,n_\varphi(\bar{\varphi})}\,, \end{aligned} \tag{32}$$

where $n_{R,i}$, $m_{R,i}$, and $n_{R,j}$, $m_{R,j}$, with i and j running from A to P, are critical pairs of normal force and bending moment lying on the failure surface associated with the shell segment generator. The remaining failure surface is defined by a polygon set up by the aforementioned points, e.g. $i = B$ and $j = C$ define the starting point and the end point of one line segment of the aforementioned polygon, as indicated in Fig. 9.

The location of the individual polygonal vertices in the force-moment plane is governed by characteristic deformation states, see Figs. 10 and 11, such as: (i) the entire cross-section is compressed (associated with point A in Fig. 9), or (ii) the neutral line passes through the center of gravity of the internal reinforcement (associated with point B in Fig. 9). This is cast in a mathematical form, as given in Table 6 for all points A to P. In this context, the compressive strain of shotcrete at the (compressive) strength limit amounts to $\varepsilon_{c2} = 2.0‰$, the maximum compressive strain of shotcrete amounts to $\varepsilon_{cu2} = 3.5‰$, and the yield strain of the reinforcement amounts to $\varepsilon_{sy} = 2.3915‰$. The latter results from f_{yd}/E_s, with the yield strength of the reinforcement $f_{yd} = 478.3\,\text{MPa}$, and with the elastic modulus of the reinforcement $E_s = 200\,000\,\text{MPa}$. The corresponding generator-specific load-bearing capacity is determined according to Eurocode 2 (ÖNORM EN 1992-1-1, 2015). Accordingly, the resistance of the normal forces (per unit length) is given as

$$n_R(t) = a_{s,o}\,\sigma_{s,o} - x_B\,f_b(t) + a_{s,i}\,\sigma_{s,i}\,, \tag{33}$$

and the resistance of the bending moments (per unit length) is given as

$$m_R(t) = a_{s,o}\,\sigma_{s,o}\,r_{s,o} \pm x_B\,f_b(t)\,r_c - a_{s,i}\,\sigma_{s,i}\,r_{s,i}\,, \tag{34}$$

with the cross-sectional area of the inner and the outer, circumferentially oriented reinforcement per unit length in tunnel driving direction, $a_{s,i}$, $a_{s,o}$, the steel stresses $\sigma_{s,i}$, $\sigma_{s,o}$ (which are specific to the points A to P in Fig. 9), and the distances to the shell midsurface $r_{s,i}$, $r_{s,o}$; the height of the concrete compression zone x_B (which is also specific to the points A to P in Fig. 9), its distance from the shell midsurface $r_c = \left(h - x_B\right)/2$, and with the biaxial compressive strength of the shotcrete f_b considered as a positive value, i.e. $f_b(t) > 0$. The latter is given by

$$f_b(t) = \kappa\,f_c(t)\,, \tag{35}$$

with f_c as the uniaxial compressive strength of shotcrete, and with κ as the ratio of biaxial to uniaxial compressive strength of shotcrete, $\kappa = 1.15$ following from standard tests (Kupfer, 1973). Under isothermal conditions at 20 centigrades, the temporal evolution of the uniaxial strength of concrete can be approximated through (CEB-FIB, 2010; Scharf et al., 2022)

$$f_c(t) = f_{c,28d}\exp\left[s_E\left(1-\sqrt{\frac{28\,\text{days}}{t}}\right)\right]. \tag{36}$$

Typical values relevant for shotcrete are given in Tables 4 and 5.

$\mathcal{U}(\bar{\varphi},t)$ may well reach values of one at specific locations of the measurement cross-section. Then, a plastic hinge may start to be formed. The latter has the following characteristics: (i) the bending moment associated with reaching $\mathcal{U}(\bar{\varphi},t) = 1+\varepsilon,\quad 0<\varepsilon\ll 1$, is considered as a plastic bending moment m_z^p, (ii) (compressive) normal forces can still be transmitted and evolve independently, affecting the magnitude of the current plastic bending moment, and (iii) a jump (discontinuity) in the rotational angle of the shell generators, denoted as $[\![\theta_z^M]\!]_k$, is allowed, see Fig. 12. This jump at location $\bar{\varphi}_k$ implies the following mathematical format of the distribution of rotational angles along the shell segment,

$$\theta_{z,k}^M(\bar{\varphi},t) = [\![\theta_z^M]\!]_k(t)\,H(\bar{\varphi}-\bar{\varphi}_k)\,, \tag{37}$$

and these jumps appear in the rate Eqs. (13)–(15). In addition, the development of the plastic hinge-induced jump in generator rotation

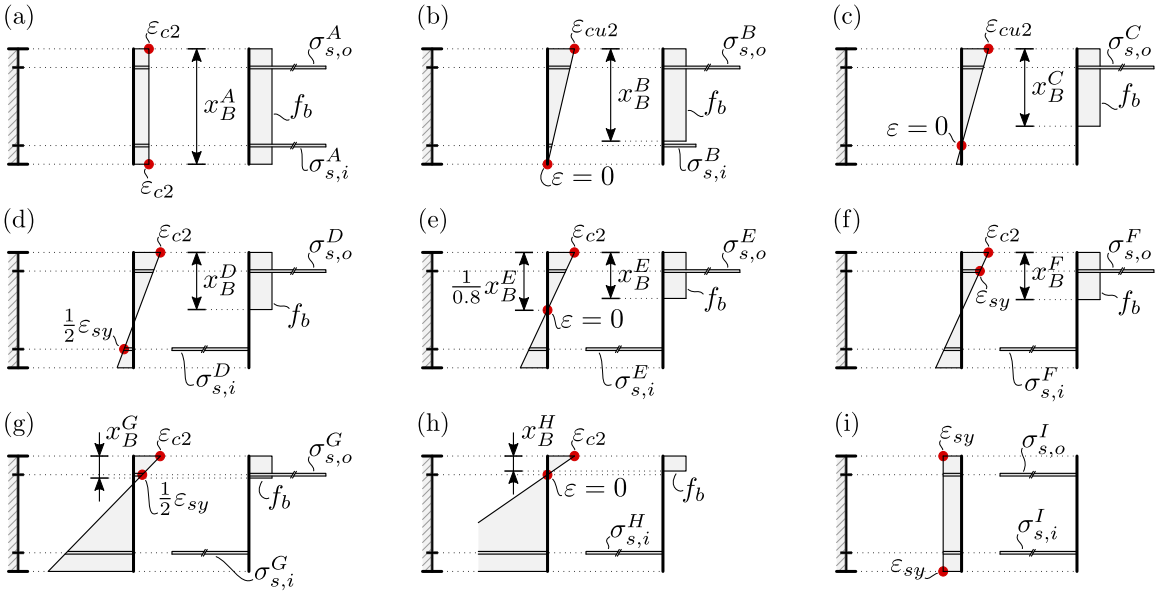

Fig. 10. Deformation states associated with the points *A*, *B*, *C*, *D*, *E*, *F*, *G*, *H*, and *I* of the interaction diagram of Fig. 9; characterized by negative bending moment around the $\mathbf{e}_z$-axis, and defined through two strain values marked in red, together with corresponding stress profiles.. (For interpretation of the references to color in this figure legend, the reader is referred to the web version of this article.)

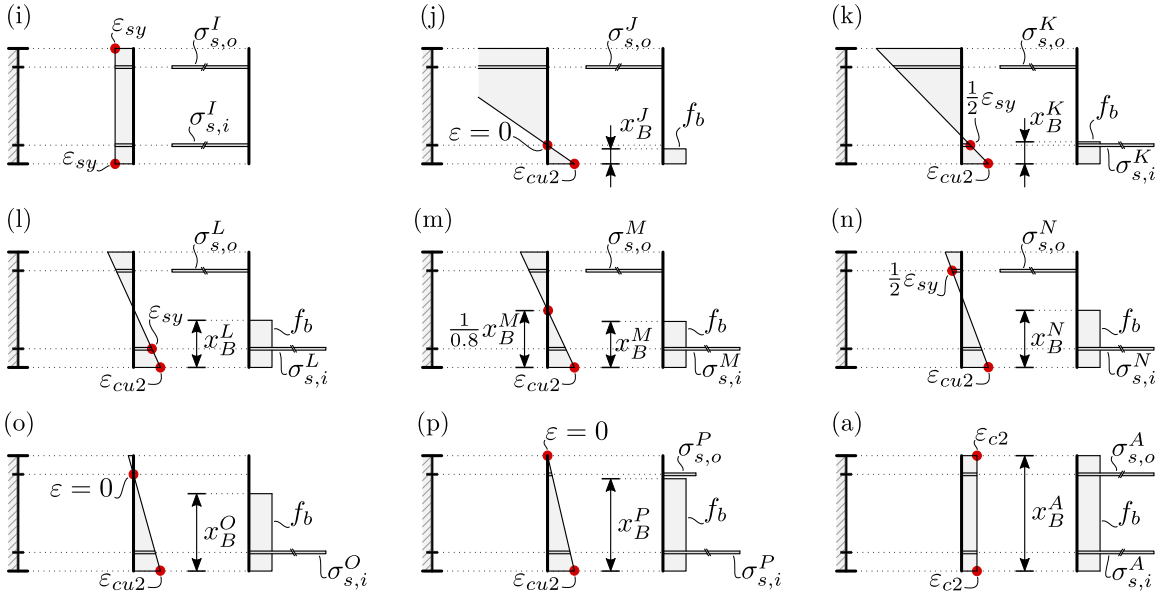

Fig. 11. Deformation states associated with the points *I*, *J*, *K*, *L*, *M*, *N*, *O*, *P*, and *A* of the interaction diagram of Fig. 9; characterized by positive bending moment around the $\mathbf{e}_z$-axis, and defined through two strain values marked in red, together with corresponding stress profiles. (For interpretation of the references to color in this figure legend, the reader is referred to the web version of this article.)

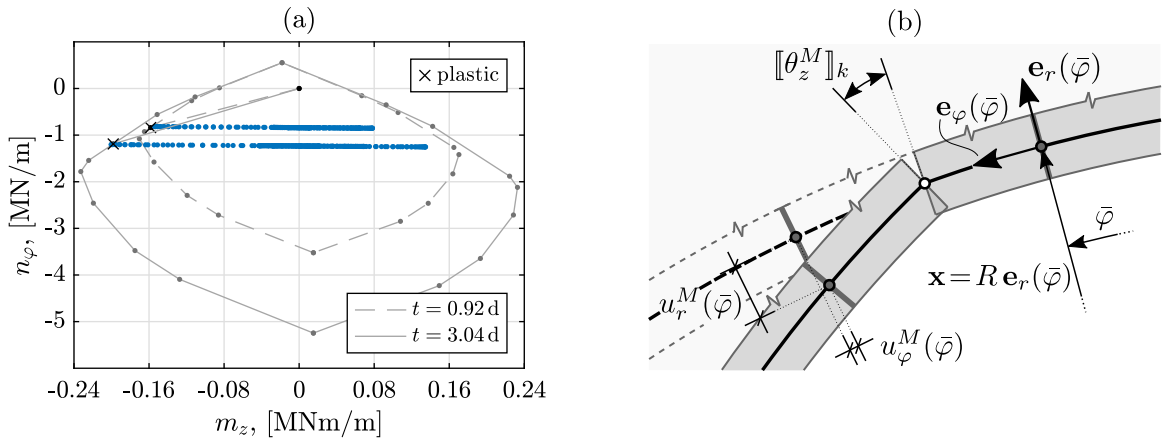

Fig. 12. Interaction diagrams for normal forces and bending moments, associated with a plastic hinge formed at $t = 0.92$ d, as well as at a subsequent time instant, $t = 3.04$ d (a); and structural model with plastic hinge: Discontinuity in angle of rotation, $[\![\theta_z^M]\!]_k$, together with radial and circumferential displacements, u_r^M and u_φ^M (b).

Table 6
Characteristics of the individual points of the interaction diagram, denoted by A to P: Height of the concrete compression zone x_B, and steel stresses of the inner and the outer, circumferentially oriented reinforcement, $\sigma_{s,i}$, $\sigma_{s,o}$.

Points	Height x_B	Steel stress $\sigma_{s,i}$	Steel stress $\sigma_{s,o}$
A	h	$-\varepsilon_{c2}\,E_s/10^3$	$-\varepsilon_{c2}\,E_s/10^3$
B	$0.8\,h$	$-r_5\,\varepsilon_{cu2}\,E_s/10^3$	$-\varepsilon_{sy}\,E_s/10^3$
C	$0.8\,r_1$	0	$-\varepsilon_{sy}\,E_s/10^3$
D	$\frac{0.8\,\varepsilon_{cu2}}{\varepsilon_{cu2}+\varepsilon_{sy}/2}\,r_1$	$+(\varepsilon_{sy}/2)\,E_s/10^3$	$-\varepsilon_{sy}\,E_s/10^3$
E	$\frac{0.8\,\varepsilon_{cu2}}{\varepsilon_{cu2}+\varepsilon_{sy}}\,r_1$	$+\varepsilon_{sy}\,E_s/10^3$	$-\varepsilon_{sy}\,E_s/10^3$
F	$\frac{0.8\,\varepsilon_{cu2}}{\varepsilon_{cu2}-\varepsilon_{sy}}\,r_2$	$+\varepsilon_{sy}\,E_s/10^3$	$-\varepsilon_{sy}\,E_s/10^3$
G	$\frac{0.8\,\varepsilon_{cu2}}{\varepsilon_{cu2}-\varepsilon_{sy}/2}\,r_2$	$+\varepsilon_{sy}\,E_s/10^3$	$-(\varepsilon_{sy}/2)\,E_s/10^3$
H	$0.8\,r_2$	$+\varepsilon_{sy}\,E_s/10^3$	0
I	0	$+\varepsilon_{sy}\,E_s/10^3$	$+\varepsilon_{sy}\,E_s/10^3$
J	$0.8\,r_3$	0	$+\varepsilon_{sy}\,E_s/10^3$
K	$\frac{0.8\,\varepsilon_{cu2}}{\varepsilon_{cu2}-\varepsilon_{sy}/2}\,r_3$	$-(\varepsilon_{sy}/2)\,E_s/10^3$	$+\varepsilon_{sy}\,E_s/10^3$
L	$\frac{0.8\,\varepsilon_{cu2}}{\varepsilon_{cu2}-\varepsilon_{sy}}\,r_3$	$-\varepsilon_{sy}\,E_s/10^3$	$+\varepsilon_{sy}\,E_s/10^3$
M	$\frac{0.8\,\varepsilon_{cu2}}{\varepsilon_{cu2}+\varepsilon_{sy}}\,r_4$	$-\varepsilon_{sy}\,E_s/10^3$	$+\varepsilon_{sy}\,E_s/10^3$
N	$\frac{0.8\,\varepsilon_{cu2}}{\varepsilon_{cu2}+\varepsilon_{sy}/2}\,r_4$	$-\varepsilon_{sy}\,E_s/10^3$	$+(\varepsilon_{sy}/2)\,E_s/10^3$
O	$0.8\,r_4$	$-\varepsilon_{sy}\,E_s/10^3$	0
P	$0.8\,h$	$-\varepsilon_{sy}\,E_s/10^3$	$-r_6\,\varepsilon_{cu2}\,E_s/10^3$
with	$r_1 = r_{s,i} + h/2,\ r_2 = h/2 - r_{s,o},\ r_3 = h/2 - r_{s,i},$		
	$r_4 = r_{s,o} + h/2,\ r_5 = (h/2 - r_{s,i})/h,\ r_6 = (h/2 - r_{s,o})/h$		

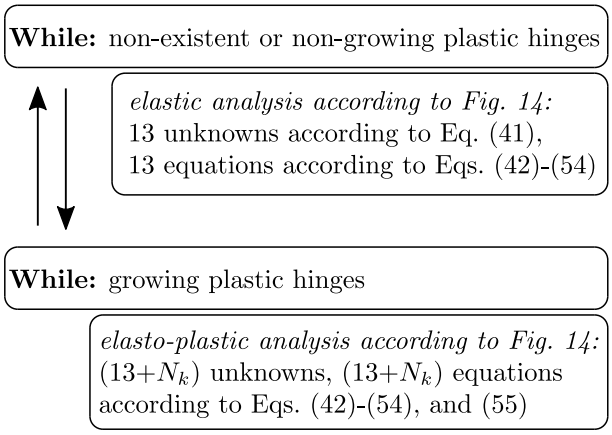

Fig. 13. Flow chart summarizing systems of equations for ground pressure as well as impost force and moments.

$[\![\theta_z^M]\!]_k(\bar\varphi_k, t)$, i.e. the description of the underlying plastic process, is based on an evolution law that can be linked to the following loading stages,

- $\mathcal{U}(\bar\varphi, t) = 1 + \varepsilon\ ;\ \ [\![\dot\theta_z^M]\!]_k > 0\ \ \rightarrow$ plastic loading,
- $\mathcal{U}(\bar\varphi, t) = 1 + \varepsilon\ ;\ \ [\![\dot\theta_z^M]\!]_k = 0\ \ \rightarrow$ neutral load,
- $\mathcal{U}(\bar\varphi, t) < 1\ ;\ \ [\![\dot\theta_z^M]\!]_k = 0\ \ \rightarrow$ elastic loading, or unloading.

In detail, loading and unloading paths are shown and discussed in a $[\![\theta_z^M]\!]_k$-m_z coordinate system in the application example tunnel Stein, see Figs. 15 and 19.

5. Displacement-to-force conversion

In order to convert, by means of the kinematic evolution Eqs. (13)–(15), measured displacement values into a temporal sequence of impost force and ground pressure values, we adopt the discretization scheme of Scharf et al. (2022, 2024): All rates, i.e. temporal derivatives, occurring in the aforementioned equations are estimated from a linear evolution of the displacement and force variables between two points in time, namely between t_{n-1} and t_n, so that the displacement–force

relations associated with each time instant t_n, $n = 1, \dots, N_t$, take the following format:

$$
\begin{aligned}
&+\frac{u_r^M(\bar{\varphi},t_n)-u_r^M(\bar{\varphi},t_{n-1})}{\Delta t_n}-\frac{u_{r,RI}^M(t_n)-u_{r,RI}^M(t_{n-1})}{\Delta t_n\,\cos(\bar{\varphi})^{-1}}\\
&-\frac{u_{\varphi,RI}^M(t_n)-u_{\varphi,RI}^M(t_{n-1})}{\Delta t_n\,\sin(\bar{\varphi})^{-1}}+\frac{R\,\theta_{z,RI}^M(t_n)-R\,\theta_{z,RI}^M(t_{n-1})}{\Delta t_n\,\sin(\bar{\varphi})^{-1}}\\
&-\sum_{k=1}^{N_k}\mathcal{I}_{z,k\to r}(\bar{\varphi})\times H[\mathcal{U}(\bar{\varphi},t)-1]\\
&\qquad\times\left\{\frac{R\,[\![\theta_z^M]\!]_k(t_n)-R\,[\![\theta_z^M]\!]_k(t_{n-1})}{\Delta t_n}\right\}\\
&-\mathcal{I}_{N\to r}(\bar{\varphi})\left\{\sum_{m=1}^{N_t}\frac{\eta\big(n_\varphi(t_{n-1}),m_z(t_{n-1})\big)}{E_c\big(\xi(t_n)\big)}\frac{\beta}{t_0^*}\left[\frac{t_n-t_m}{t_0^*}\right]^{\beta-1}\right.\\
&\qquad\left.\times\Big[N_p(t_m)-N_p(t_{m-1})\Big]+\frac{N_p(t_n)-N_p(t_{n-1})}{E\big(\xi(t_n)\big)\Delta t_n}\right\}\\
&-\sum_{j=1}^{8}\mathcal{I}_{j\to r}(\bar{\varphi})\left\{\sum_{m=1}^{N_t}\frac{\eta\big(n_\varphi(t_{n-1}),m_z(t_{n-1})\big)}{E_c\big(\xi(t_n)\big)}\frac{\beta}{t_0^*}\left[\frac{t_n-t_m}{t_0^*}\right]^{\beta-1}\right.\\
&\qquad\left.\times\Big[G_{p,j}(t_m)-G_{p,j}(t_{m-1})\Big]+\frac{G_{p,j}(t_n)-G_{p,j}(t_{n-1})}{E\big(\xi(t_n)\big)\Delta t_n}\right\}\\
&=\mathcal{D}_r\Big[u_r^M(\bar{\varphi},t_n),\bar{\varphi}\Big]=0,
\end{aligned}
\tag{38}
$$

$$
\begin{aligned}
&+\frac{u_\varphi^M(\bar{\varphi},t_n)-u_\varphi^M(\bar{\varphi},t_{n-1})}{\Delta t_n}+\frac{u_{r,RI}^M(t_n)-u_{r,RI}^M(t_{n-1})}{\Delta t_n\,\sin(\bar{\varphi})^{-1}}\\
&-\frac{u_{\varphi,RI}^M(t_n)-u_{\varphi,RI}^M(t_{n-1})}{\Delta t_n\,\cos(\bar{\varphi})^{-1}}+\frac{R\,\theta_{z,RI}^M(t_n)-R\,\theta_{z,RI}^M(t_{n-1})}{\Delta t_n\big(\cos(\bar{\varphi})-1\big)^{-1}}\\
&-\sum_{k=1}^{N_k}\mathcal{I}_{z,k\to\varphi}(\bar{\varphi})\times H[\mathcal{U}(\bar{\varphi},t)-1]\\
&\qquad\times\left\{\frac{R\,[\![\theta_z^M]\!]_k(t_n)-R\,[\![\theta_z^M]\!]_k(t_{n-1})}{\Delta t_n}\right\}\\
&-\mathcal{I}_{N\to\varphi}(\bar{\varphi})\left\{\sum_{m=1}^{N_t}\frac{\eta\big(n_\varphi(t_{n-1}),m_z(t_{n-1})\big)}{E_c\big(\xi(t_n)\big)}\frac{\beta}{t_0^*}\left[\frac{t_n-t_m}{t_0^*}\right]^{\beta-1}\right.\\
&\qquad\left.\times\Big[N_p(t_m)-N_p(t_{m-1})\Big]+\frac{N_p(t_n)-N_p(t_{n-1})}{E\big(\xi(t_n)\big)\Delta t_n}\right\}\\
&-\sum_{j=1}^{8}\mathcal{I}_{j\to\varphi}(\bar{\varphi})\left\{\sum_{m=1}^{N_t}\frac{\eta\big(n_\varphi(t_{n-1}),m_z(t_{n-1})\big)}{E_c\big(\xi(t_n)\big)}\frac{\beta}{t_0^*}\left[\frac{t_n-t_m}{t_0^*}\right]^{\beta-1}\right.\\
&\qquad\left.\times\Big[G_{p,j}(t_m)-G_{p,j}(t_{m-1})\Big]+\frac{G_{p,j}(t_n)-G_{p,j}(t_{n-1})}{E\big(\xi(t_n)\big)\Delta t_n}\right\}\\
&=\mathcal{D}_\varphi\Big[u_\varphi^M(\bar{\varphi},t_n),\bar{\varphi}\Big]=0,
\end{aligned}
\tag{39}
$$

$$
\begin{aligned}
&+\frac{\theta_z^M(\bar{\varphi},t_n)-\theta_z^M(\bar{\varphi},t_{n-1})}{\Delta t_n}-\frac{\theta_{z,RI}^M(t_n)-\theta_{z,RI}^M(t_{n-1})}{\Delta t_n}\\
&-\sum_{k=1}^{N_k}H(\bar{\varphi}-\bar{\varphi}_k)\times H[\mathcal{U}(\bar{\varphi},t)-1]\\
&\qquad\times\left\{\frac{[\![\theta_z^M]\!]_k(t_n)-[\![\theta_z^M]\!]_k(t_{n-1})}{\Delta t_n}\right\}\\
&-\mathcal{I}_{N\to z}(\bar{\varphi})\left\{\sum_{m=1}^{N_t}\frac{\eta\big(n_\varphi(t_{n-1}),m_z(t_{n-1})\big)}{E_c\big(\xi(t_n)\big)}\frac{\beta}{t_0^*}\left[\frac{t_n-t_m}{t_0^*}\right]^{\beta-1}\right.\\
&\qquad\left.\times\Big[N_p(t_m)-N_p(t_{m-1})\Big]+\frac{N_p(t_n)-N_p(t_{n-1})}{E\big(\xi(t_n)\big)\Delta t_n}\right\}\\
&-\sum_{j=1}^{8}\mathcal{I}_{j\to z}(\bar{\varphi})\left\{\sum_{m=1}^{N_t}\frac{\eta\big(n_\varphi(t_{n-1}),m_z(t_{n-1})\big)}{E_c\big(\xi(t_n)\big)}\frac{\beta}{t_0^*}\left[\frac{t_n-t_m}{t_0^*}\right]^{\beta-1}\right.\\
&\qquad\left.\times\Big[G_{p,j}(t_m)-G_{p,j}(t_{m-1})\Big]+\frac{G_{p,j}(t_n)-G_{p,j}(t_{n-1})}{E\big(\xi(t_n)\big)\Delta t_n}\right\}\\
&=\mathcal{D}_z\Big[\theta_z^M(\bar{\varphi},t_n),\bar{\varphi}\Big]=0,
\end{aligned}
\tag{40}
$$

with the time intervals $\Delta t_n = t_n - t_{n-1}$, and with the affinity factor η being evaluated for the normal force and the bending moment of the previous time instant t_{n-1}, because the corresponding force quantities for the current time instant t_n are not yet known. Rather, these force quantities will result from the Eqs. (38)–(40), as described next.

In the cases of non-existent or non-growing plastic hinges, the Eqs. (38)–(40) contain thirteen unknowns:

$$
\begin{aligned}
&G_{p,1}(t_n), G_{p,2}(t_n), G_{p,3}(t_n), G_{p,4}(t_n),\\
&G_{p,5}(t_n), G_{p,6}(t_n), G_{p,7}(t_n), G_{p,8}(t_n),\\
&N_p(t_n),\\
&u_{r,RI}^M(t_n), u_{\varphi,RI}^M(t_n), \theta_{z,RI}^M(t_n), \theta_{z,LI}^M(t_n).
\end{aligned}
\tag{41}
$$

For the determination of these unknowns, thirteen equations are necessary, see also the flow chart of Fig. 13. They are obtained as follows

- Two equations result from insertion of the moment distribution according to Eq. (11), into the natural boundary conditions (12). They read as

$$
-N_p\,\frac{\mathrm{d}\mathcal{I}_{N\to f}(\bar{\varphi}=0)}{\mathrm{d}\bar{\varphi}}+\sum_{i=1}^{8}R\,G_{p,i}\,\frac{\mathrm{d}\mathcal{I}_{i\to f}(\bar{\varphi}=0)}{\mathrm{d}\bar{\varphi}}\;=\;0\,,
\tag{42}
$$

$$
-N_p\frac{\mathrm{d}\mathcal{I}_{N\to f}(\bar{\varphi}=\Delta\varphi)}{\mathrm{d}\bar{\varphi}}+\sum_{i=1}^{8}RG_{p,i}\,\frac{\mathrm{d}\mathcal{I}_{i\to f}(\bar{\varphi}=\Delta\varphi)}{\mathrm{d}\bar{\varphi}}\;=\;0\,,
\tag{43}
$$

  with the (external)-traction-to-(internal)-force influence functions derived with respect to the circumferential direction and specified for the right and left impost, respectively; the corresponding mathematical expressions are given as Eqs. (59)–(66) in the Appendix B.
- Five equations result from specification of the temporally evolving fields of radial displacements according to Eq. (38), for the corresponding measurements conducted at MP1 to MP5; they read as

$$
\mathcal{D}_r\Big[u_r^M(\bar{\varphi}_1,t_n)=u_r^{\mathrm{MP1}}(t_n),\bar{\varphi}_1\Big]=0\,,
\tag{44}
$$

$$
\mathcal{D}_r\Big[u_r^M(\bar{\varphi}_2,t_n)=u_r^{\mathrm{MP2}}(t_n),\bar{\varphi}_2\Big]=0\,,
\tag{45}
$$

$$
\mathcal{D}_r\Big[u_r^M(\bar{\varphi}_3,t_n)=u_r^{\mathrm{MP3}}(t_n),\bar{\varphi}_3\Big]=0\,,
\tag{46}
$$

$$
\mathcal{D}_r\Big[u_r^M(\bar{\varphi}_4,t_n)=u_r^{\mathrm{MP4}}(t_n),\bar{\varphi}_4\Big]=0\,,
\tag{47}
$$

$$
\mathcal{D}_r\Big[u_r^M(\bar{\varphi}_5,t_n)=u_r^{\mathrm{MP5}}(t_n),\bar{\varphi}_5\Big]=0\,,
\tag{48}
$$

  whereby the histories of the radial displacements of the measurement points MP1 to MP5, i.e. $u_r^{\mathrm{MP1}}(t)$, $u_r^{\mathrm{MP2}}(t)$, $u_r^{\mathrm{MP3}}(t)$, $u_r^{\mathrm{MP4}}(t)$, $u_r^{\mathrm{MP5}}(t)$, are expressed in terms of the fitting functions given by Eqs. (1) and (2) and depicted in Fig. 5(a-e).
- Five equations result from specification of the temporally evolving fields of tangential displacements according to Eq. (39) for the corresponding measurements conducted at MP1 to MP5; they read as

$$
\mathcal{D}_\varphi\Big[u_\varphi^M(\bar{\varphi}_1,t_n)=u_\varphi^{\mathrm{MP1}}(t_n),\bar{\varphi}_1\Big]=0\,,
\tag{49}
$$

$$
\mathcal{D}_\varphi\Big[u_\varphi^M(\bar{\varphi}_2,t_n)=u_\varphi^{\mathrm{MP2}}(t_n),\bar{\varphi}_2\Big]=0\,,
\tag{50}
$$

$$
\mathcal{D}_\varphi\Big[u_\varphi^M(\bar{\varphi}_3,t_n)=u_\varphi^{\mathrm{MP3}}(t_n),\bar{\varphi}_3\Big]=0\,,
\tag{51}
$$

$$
\mathcal{D}_\varphi\Big[u_\varphi^M(\bar{\varphi}_4,t_n)=u_\varphi^{\mathrm{MP4}}(t_n),\bar{\varphi}_4\Big]=0\,,
\tag{52}
$$

$$
\mathcal{D}_\varphi\Big[u_\varphi^M(\bar{\varphi}_5,t_n)=u_\varphi^{\mathrm{MP5}}(t_n),\bar{\varphi}_5\Big]=0\,,
\tag{53}
$$

  whereby the histories of the tangential displacements of the measurement points MP1 to MP5, i.e. $u_\varphi^{\mathrm{MP1}}(t)$, $u_\varphi^{\mathrm{MP2}}(t)$, $u_\varphi^{\mathrm{MP3}}(t)$, $u_\varphi^{\mathrm{MP4}}(t)$, $u_\varphi^{\mathrm{MP5}}(t)$, are expressed in terms of the fitting functions given by Eqs. (1) and (2) and depicted in Fig. 5(a-e).

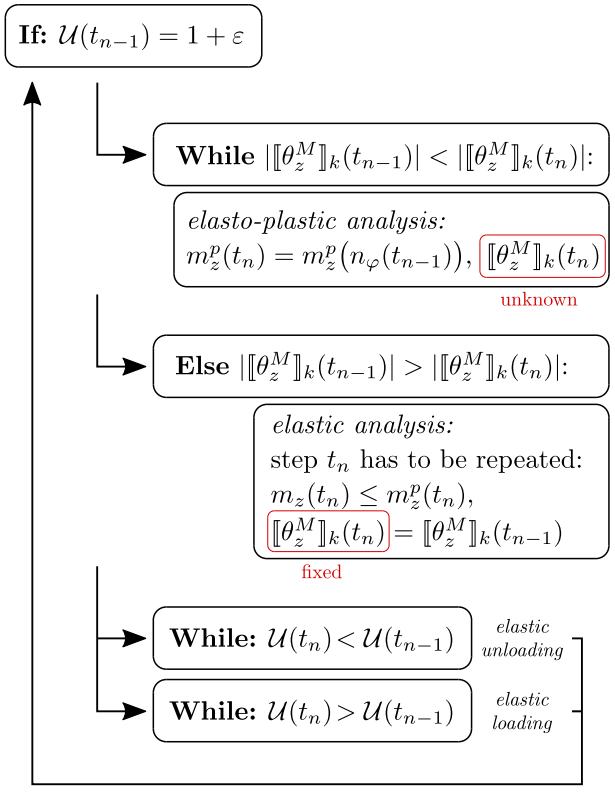

Fig. 14. Flow chart for a plastic hinge.

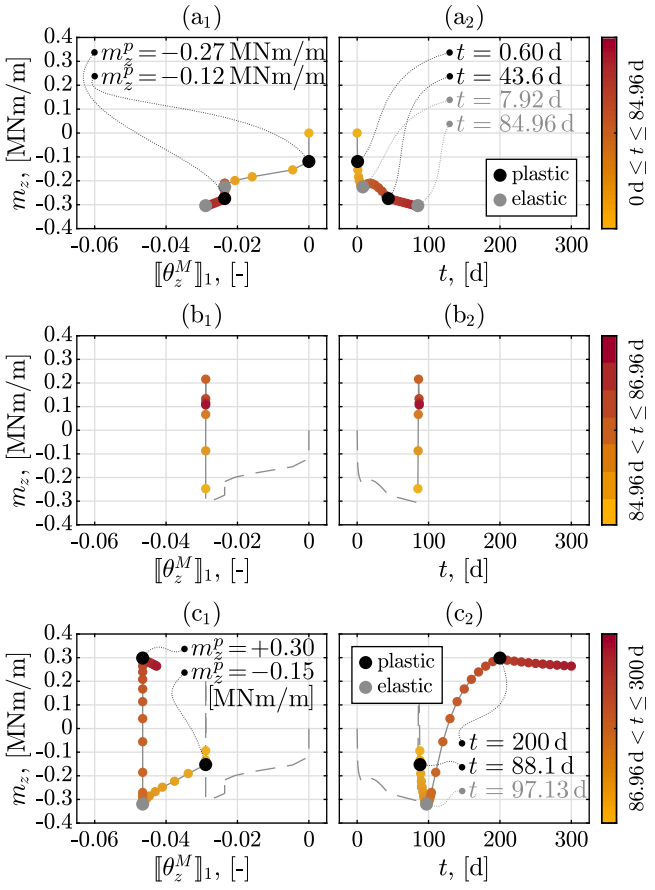

Fig. 15. Color-defined temporal evolution of the bending moment at plastic hinge #1, as a function of the plastic angle of rotation (a_1,b_1,c_1) and over time (a_2,b_2,c_2): (a) construction phase CP1, lasting from $t = 0$ d to $t = 84.96$ d, (b) construction phase CP2, lasting from $t = 84.96$ d to $t = 86.96$ d, and (c) construction phase CP3, lasting from $t = 86.96$ d to $t = 300$ d. (For interpretation of the references to color in this figure legend, the reader is referred to the web version of this article.)

- And one equation results from specification of the temporally evolving field of rotation angles according to Eq. (40), for the unknown $\theta^M_{z,LI}(t_n)$; it reads as

$$\mathcal{D}_z\left[\theta_z^M(\bar{\varphi} = \Delta\varphi, t_n) = \theta^M_{z,LI}(t_n), \bar{\varphi} = \Delta\varphi\right] = 0\,. \tag{54}$$

Initiation of a plastic hinge is indicated by reaching $\mathcal{U} = 1$ at one shell generator position. The corresponding bending moment is recorded as plastic moment m_z^p associated with the respective time instant, say t_{n-1}. For the next time step, a system of equations with fourteen unknowns needs to be solved, the thirteen force quantities given before, and the jump in generator rotation arising from the developing plastic hinge, denoted as $[\![\theta_z^M]\!]_1$. As additional equation, the bending moment according to Eq. (11) is set equal to the plastic bending moment, i.e. $m_z(\bar{\varphi} = \bar{\varphi}_k, t_n) = m_z^p(t_{n-1})$, so that

$$\begin{aligned} m_z^p(\bar{\varphi}_k, t_{n-1}) \;=\; & +R\,N_p(t_n)\left[1 - \mathcal{I}_{N\to f}(\bar{\varphi}_k)\right] \\ & +\sum_{i=1}^{8} R^2\,G_{p,i}(t_n)\,\mathcal{I}_{i\to f}(\bar{\varphi}_k)\,, \end{aligned} \tag{55}$$

The aforementioned fourteen equations then allow for determination of fourteen unknowns, including the jump in generator rotation arising from the developing plastic hinge, denoted as $[\![\theta_z^M]\!]_1(t_n)$.

If the norm of the latter is larger than its norm in the preceding time step, the plastic hinge has grown, and the solutions of the fourteen equations have been physically reasonable, see also the flow chart of Fig. 14. In this case, we are left with updating the value of the plastic moment, based on the latest value of axial force at the position of the plastic hinge, by means of the force-moment interaction diagram. Mathematically speaking, this reads as

$$m_z^p(t_n) = \frac{m_{R,j}\,n_{R,i} - m_{R,i}\,n_{R,j} + [m_{R,i} - m_{R,j}]\,n_\varphi(t_{n-1})}{n_{R,i} - n_{R,j}}\,, \tag{56}$$

where $n_{R,i}$, $m_{R,i}$, and $n_{R,j}$, $m_{R,j}$, as well as the normal force, are the critical resistance pairs for the time instant t_n.

However, if the norm of the jump in generator rotation associated with the plastic hinge is smaller than its norm in the preceding time step, the current time was characterized by elastic unloading. Hence, the determination of the unknown force values has to be repeated on the basis of the thirteen equations without the generator rotation jump, with $[\![\theta_z^M]\!]_1(t_{n-1})$ being fixed, see the flow chart of Fig. 14.

If several plastic hinges are indicated by several shell generators associated with $\mathcal{U} = 1$, Eq. (55) is evaluated for all the positions of these plastic hinges, $\bar{\varphi}_k$, $k = 1, 2, \ldots, N_k$, with N_k being the number of plastic hinges. This results in $(13 + N_k)$ equations, see also the flow chart of Fig. 13, needed for the determination of the thirteen unknowns given below Eq. (40) and the N_k rotational jumps $[\![\theta_z^M]\!]_k$, $k = 1, 2, \ldots, N_k$. Thereafter, the check of plastic hinge growth is made for all positions $\bar{\varphi}_k$, $k = 1, 2, \ldots, N_k$, followed by either plastic moment updating according to Eq. (56), or by solving a smaller system of equations in case elastic unloading events have been detected.

6. Results

Realization of the displacement-to-force conversion scheme of Section 5, together with the viscoelastic–plastic constitutive framework of Section 4, reveals the following load-carrying and deformational characteristics of cross section KMA5.3.000201 of tunnel Stein:

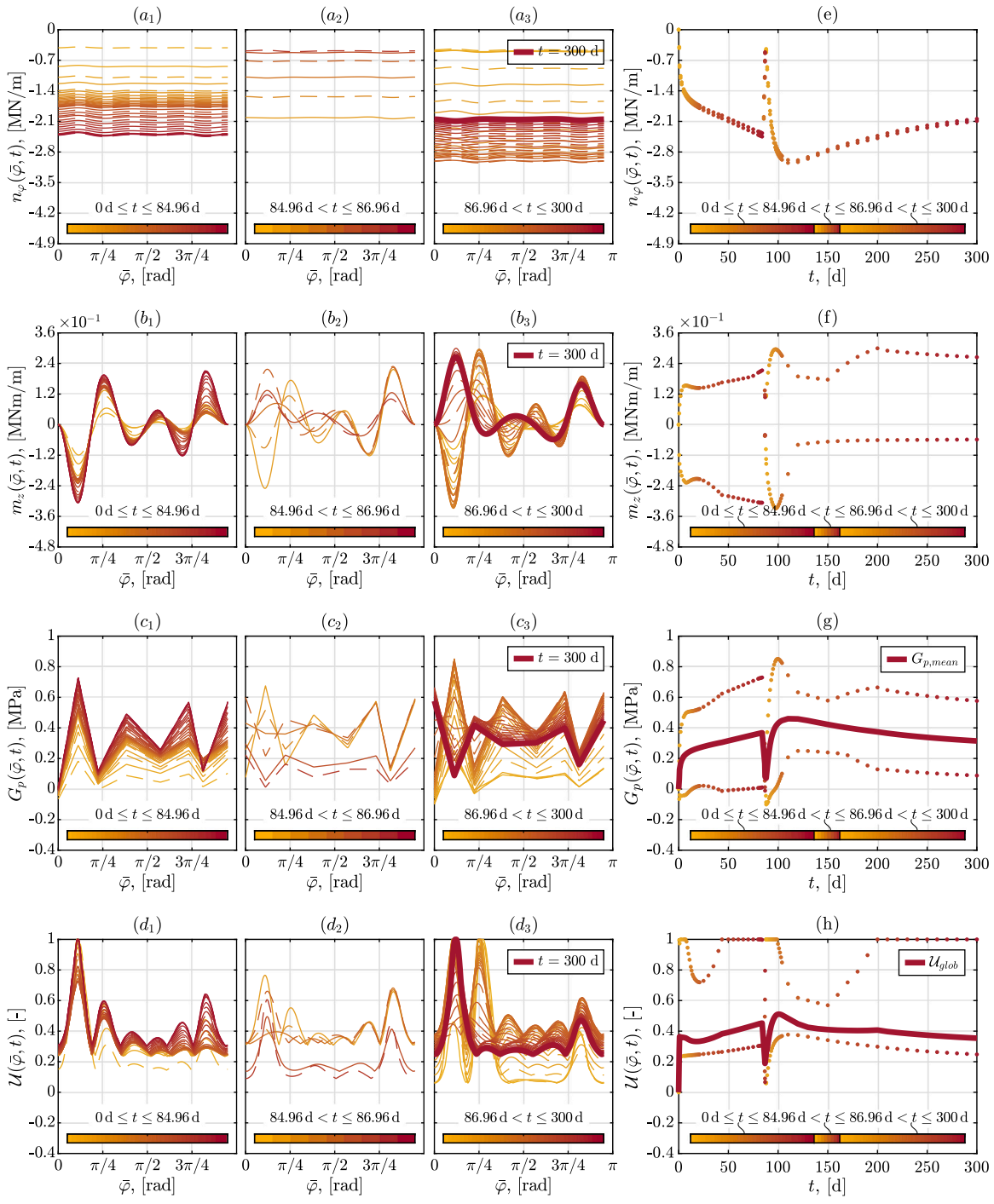

Fig. 16. Distribution of circumferential normal forces (a), bending moments (b), ground pressure (c), and degree of utilization (d) along the circumference of the top heading and associated with construction phases CP1, CP2, and CP3 (index 1-3) of tunnel Stein at measurement cross section KMA5.3.000201, and the temporal evolution of maximum and minimum values (e-h); computed from displacement measurements at MP1 through MP5.

During construction phase CP1, including construction steps #1 and #2, i.e. the installation of the top heading, the top heading feet, and the temporal top heading invert arch, and lasting from $t = 0\,\mathrm{d}$ to $t = 84.96\,\mathrm{d}$, the circumferential normal forces, while being pseudo-uniformly distributed along the tunnel shell segment, are continuously increasing with time, see Fig. 16(a_1) and (e). This evolution is linked to an increase of the ground pressure acting on the tunnel shell, see Fig. 16(g). This increase, however, comes with an increasingly non-uniform distribution of the ground pressure, showing several maxima and minima, see Fig. 16(c_1). Such a distribution, in turn, is consistent with wave-type bending moment distributions, see Fig. 16(b_1), exhibiting alternately positive and negative signs, being associated with a decrease and an increase in shell curvature, respectively. The magnitude of these bending moments also increases over time. Thereby, the

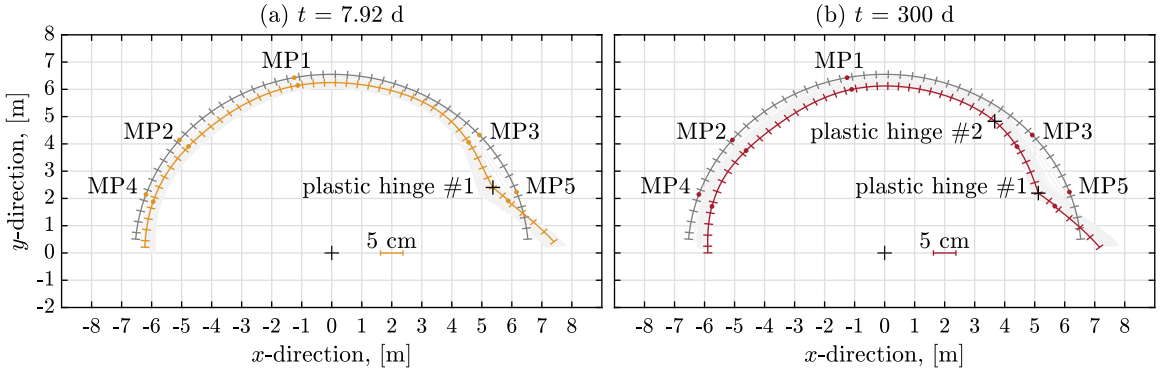

Fig. 17. Midsurface displacement distribution with corresponding shell generator lines of length h = 0.30 m, at two different time instants t, at the measurement cross-section KMA5.3.000201 of tunnel Stein, on the basis of measurement data from MP1-MP5 (magnification factor of the displacements: 15).

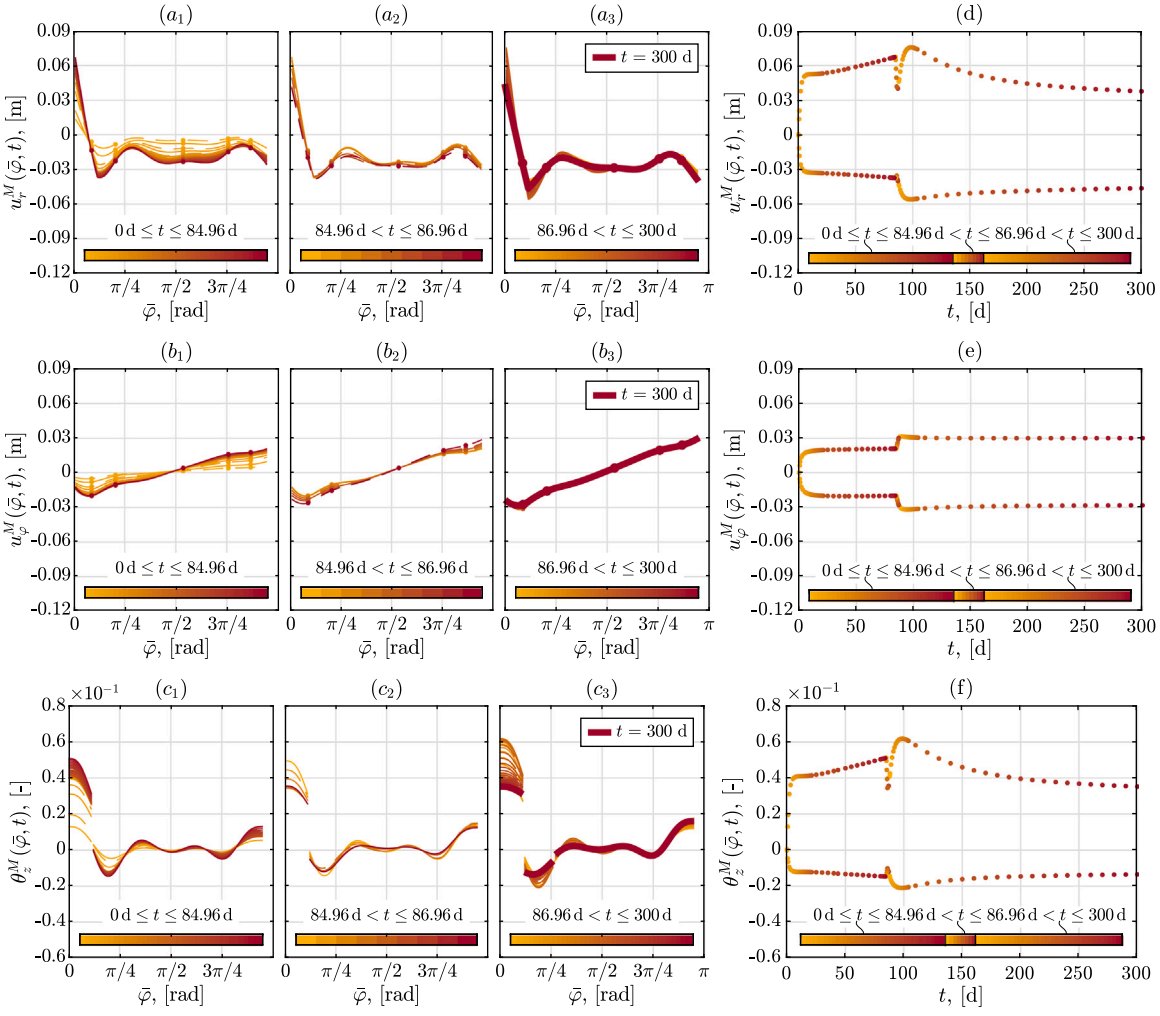

Fig. 18. Distribution of radial and circumferential displacements (a-b), and generator rotations (c) along the circumference of the top heading and associated with construction phases CP1, CP2, and CP3 (index 1-3) of tunnel Stein at measurement cross section KMA5.3.000201, and the temporal evolution of maximum and minimum values (d-f); computed from displacement measurements at MP1 through MP5.

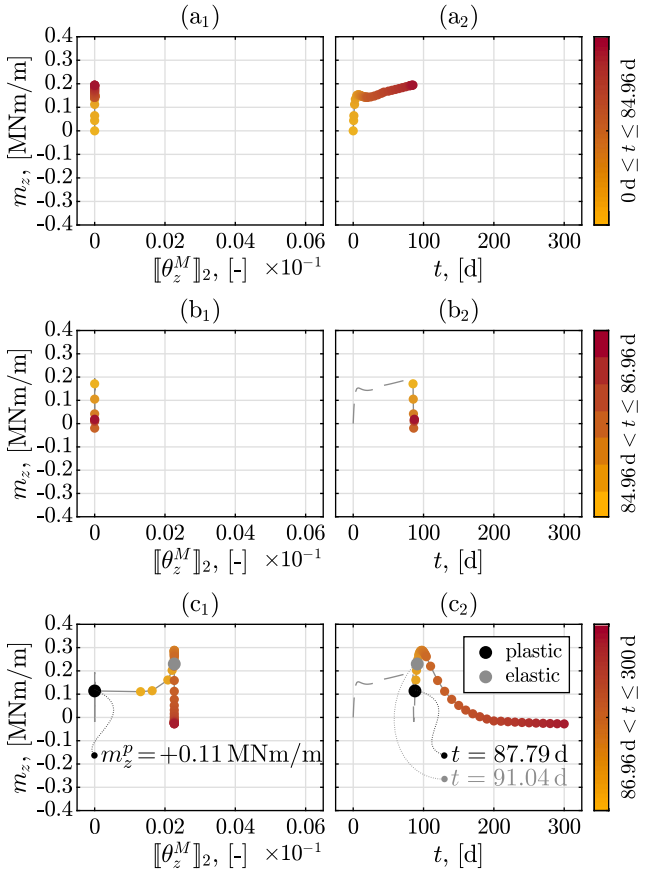

Fig. 19. Color-defined temporal evolution of the bending moment at plastic hinge #2, as a function of the plastic angle of rotation (a_1,b_1,c_1) and over time (a_2,b_2,c_2): (a) construction phase CP1, lasting from $t = 0$ d to $t = 84.96$ d, (b) construction phase CP2, lasting from $t = 84.96$ d to $t = 86.96$ d, and (c) construction phase CP3, lasting from $t = 86.96$ d to $t = 300$ d. (For interpretation of the references to color in this figure legend, the reader is referred to the web version of this article.)

bending moment with the largest absolute value, occurring close to the right impost, becomes plastic very soon, namely already at $t = 0.6$ d, see Fig. 16(d_1) and (h), as well as the right and left black dots, respectively, in Fig. 15(a_1) and (a_2), respectively. The plastic loading lasts from $t = 0.60$ d to $t = 7.92$ d, when the first load re-distribution around the freshly excavated top heading has been virtually completed, as indicated by a sharp decline in the growth of the ground pressure acting on the tunnel shell, see Fig. 16(g), being associated with virtually time-invariant ground pressure values close to the position of the formerly plastic hinge, as seen in Fig. 16(c_1). At the same time, the ongoing hydration process, with correspondingly increasing shotcrete strength values (Pichler et al., 2008), results in an enlargement of the elastic domain within the normal force-bending moment interaction diagram of Fig. 9. The respective enlargement kinetics is so pronounced that the force-moment data pair prevailing at day eight actually leaves the boundary indicating plastic limit states, and re-locates in the (growing) elastic domain, while the formerly plastic hinge remains "frozen" at the jump in generator rotation attained at $t = 7.92$ d. At the same time, the bending moments decrease slightly in magnitude, see Fig. 16(f). At about $t = 20$ d, the ground pressure starts to increase again; however, the simultaneous chemical hardening of the shotcrete, i.e. its hydration-driven strength increase (Hellmich et al., 1999b), allows for elastic accommodation of the correspondingly increasing internal forces acting within the tunnel shell. It is only at $t = 43.6$ d, with a bending moment amounting to $m_z(t = 43.6\,\text{d}) = -0.27$ MNm/m, that the plastic hinge re-develops, see the left and right blacks dots, respectively, in Fig. 15(a_1) and (a_2), respectively. Thereafter, the rotational jump keeps growing throughout the rest of construction phase CP1. The two growth phases of the plastic hinge are indicated by non-vertical lines in the bending-moment-over-jump-in-generator-rotation diagram of Fig. 15(a_1) and by a pronounced kink in the midsurface displacement profile of Fig. 17(a). The latter comes with positive, i.e. outward, radial displacements of the right foot of the top heading, while generally, the tunnel shell undergoes inwards and downwards movements, see Fig. 17(a) and Fig. 18(a_1) and (b_1). At the same time, the non-uniform ground pressure and bending moment distributions are reflected by alternating, positive as well as negative, values of the rotational angle of the shell generators, along the circumference of the tunnel shell, see Fig. 18(c_1).

Construction phase CP2, including construction steps #3, #4, and #5, i.e. the demolition of the temporal invert arch of the top heading, excavation of the bench and invert portion of the tunnel cross section as well as installation of corresponding shell components, and lasting from $t = 84.96$ d to $t = 86.96$ d, is characterized by a sudden and significant unloading of the tunnel shell of cross section KMA5.3.000201: Circumferential normal forces and ground pressures are dropping by a factor of up to five, see Fig. 16(a_2), (c_2), (e), (g), while essentially all quantities describing the loading and deformational states of the tunnel shell, such as bending moments, degree of utilization, radial displacement and rotational angle, undergo a remarkable reduction, see Fig. 16(b_2), (d_2), (f), (h) and Fig. 18(a_2), (c_2), (d), (f). In this context, the plastic hinge close to the right impost "freezes" again, and the associated bending moment not only reduces to zero, but even changes sign thereafter, see Fig. 16(b_2). The dramatic unloading during construction phase CP2 stems from the sudden loss of load carrying capacity below the feet of the top heading, due to the excavation of the benches, so that the tunnel portions ahead of KMA5.3.000201, where the feet of the top heading still carry load, and behind KMA5.3.000201, where the invert arch has already been installed, take the loads which are imposed, as ground pressure, onto KMA5.3.000201. Loss of the supporting action of the top heading feet also leads to a quick settlement of the investigated cross section, as indicated by enlarged negative and positive values of circumferential displacements, respectively, at the right and the left impost, respectively, see Fig. 18(b_2), (e).

Construction phase CP3, starting directly after ring closure, and hence completion, of cross section KMA5.3.000201 at $t = 86.96$ d, is characterized by a rapid increase of loads carried by the tunnel shell, reflected in circumferential normal forces, see Fig. 16(a_3), (e), arising from quickly growing ground pressure values, see Fig. 16(c_3), (g). This comes together with inward movement of the tunnel shell, indicated by growing radial displacement values, see Fig. 18(a_3), (d). At the same time, the bending moments at the former plastic hinge first decrease to zero, before changing signs again, and then relatively quickly re-plasticize, namely at $t = 88.10$ d, see Fig. 16(d_3), (h) and Fig. 15(c_1), (c_2). Slightly before, namely at $t = 87.79$ d, second plastic hinge, this time with positive jump in generator rotation, has formed between MP1 and MP3, see Fig. 16(d_3), (h), Fig. 17(b), and Fig. 19(c_1), (c_2). Later in construction phase CP3, our displacement-to-force conversion scheme indicates slowly decreasing ground pressure and circumferential normal force values. Thus is associated with "freezing" of both plastic hinges, whereby the bending moment associated to the first one of these eventually changes signs again, before the first plastic hinge re-plasticizes, due to the unfavorable moment-force combination arising from increasing moments and decreasing forces, at $t = 200$ d, see Fig. 15(c_1), (c_2).

7. Discussion

Evaluation of geodetic displacement measurements at five points on the inner surface of typical cross section of the top heading of the NATM tunnel Stein in the south of Austria, through an analytical viscoelastic

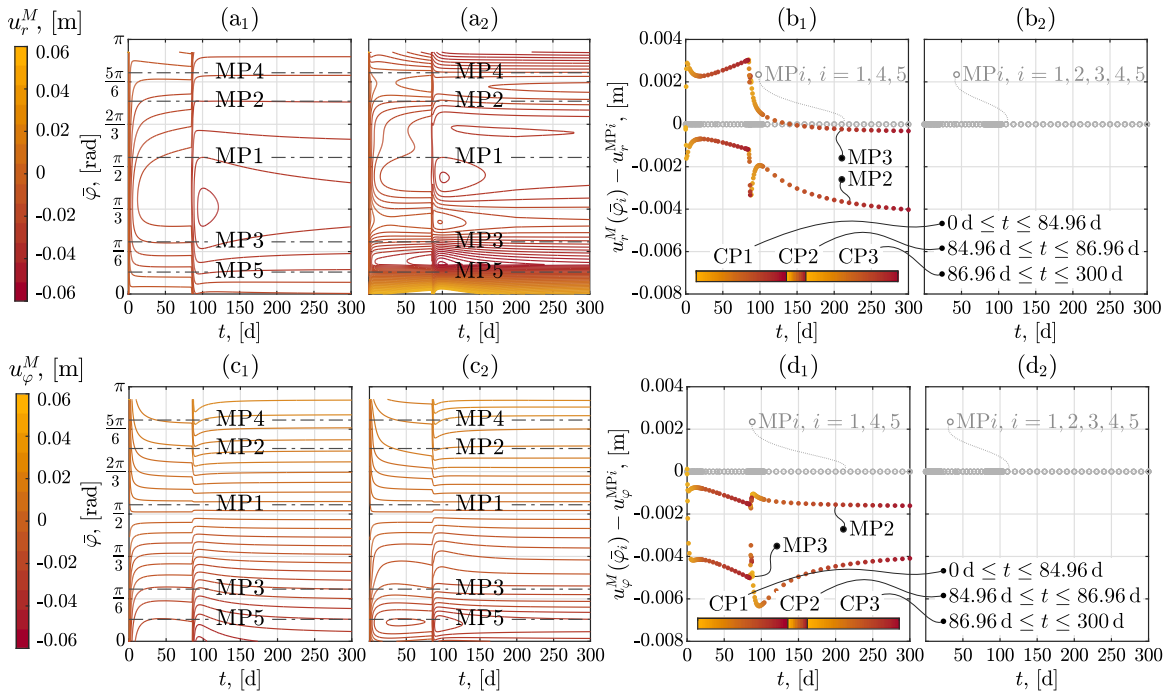

Fig. 20. Representation of the radial and tangential displacement fields over time (a,c), computed from displacement measurements at MP1, MP4, and MP5 only (a_1,c_1) and computed from displacement measurements at MP1 through MP5 (a_2,c_2); and (b,d) comparison of 3-MP-based computations (b_1,d_1) and of 5-MP-based computations (b_2,d_2), respectively, with measured field monitoring data at the measurement points MP1 to MP5 [represented in terms of a fitting function-enabled smooth evolution over time, according to Eq. (1) and (2)]..

structural mechanics model, together with plastic moment detection in line of Eurocode 2, evidenced the repeated occurrence of plastic hinges in the first 300 days of the lifetime of the investigated cross section. This greatly widens the view on NATM tunnel shells, replacing the picture of a rather monolithic solid, by the perception of a highly flexible component, which shows kind of a "segmentation" even in tunnels which do not fall into the traditional category of "segmental tunnel", i.e. those driven by tunnel boring machines (TBM) (Zhang et al., 2017; Jiang et al., 2024). Development of corresponding plastic hinges can be followed in terms of load cycles being limited by zero bending moments, see Figs. 15 and 19. Interestingly, obviously heterogeneous ground conditions around the investigated cross section KMA5.3.000201 leads to plastic bending moments and rotational jumps quantifying plastic hinges, which are not restricted to a particular direction or sign.

The non-uniform distribution of ground pressure which was reconstructed for the end of the recording period, i.e. for $t = 300\,\mathrm{d}$, characterized by two pronounced minima as seen in Fig. 16(c_3), is consistent with the action of the rock bolts seen in Fig. 3: They carry tensile forces, which are not explicitly introduced into the structural mechanics model, and hence, as a somewhat "smeared" portion of the ground pressure, reduce the latter in magnitude.

It is also very interesting to note that the detection of plastic bending moments necessitates the consideration of the data collected from all five measurements points. When restricting the analysis to the classical selection of three measurement points as widely discussed in earlier contributions (Hellmich et al., 1999a, 2001, 2020; Brandtner et al., 2007; Ullah et al., 2010; Scharf et al., 2022, 2024), namely to MP1, MP4, and MP5, the aforementioned heterogeneous ground pressure distribution is not detected, see Figs. 21–23. This is consistent with the correspondingly predicted displacements at MP2 and MP3 deviating significantly from the actual measurements, see Fig. 20. Conclusively, the number of installed measurement points is key to the realistic assessment of the load carrying behavior of NATM tunnel shells. In other words, the increased number of measurement points does not merely increase the precision of the hybrid analysis, but reveals fundamentally new features of the load carrying behavior of NATM tunnel shells. While the analysis based on three measurement points proposes the tunnel shell to act as a monolithic solid block, it is the analysis based on five measurement points, which reveals the existence of plastic hinges, i.e. that of a much more flexible structural configuration.

Further increase of the realism of the used mechanical model may concern the long-term creep behavior, which may be overestimated by the power-law creep function employed in the present context. Adoption of a logarithmic formulation for the long-term creep period may propose a less pronounced decrease in ground pressure as reported herein, or even rather constant quasi-asymptotic ground pressure states long after tunnel installation, as recently shown for segmental tunnel linings (Razgordanisharahi et al., 2024). However, this topic goes clearly beyond the scope of the present paper, which was about elucidating the pronounced bending flexibility of an NATM tunnel shell. From a more general perspective, the present paper has widened the repertoire of analytical approaches providing deep and efficient insight into the functioning of different tunneling methods (Ieronymaki et al., 2018). Thereby, we note that the current study with the refined hybrid structural analysis is restricted to the top heading sections of an NATM tunnel; it is also restricted to tunnel shells with constant radius and constant thickness. However, the presented ideas concerning plastic hinges and analytical structural modeling can be naturally extended towards shells with varying thickness and radii. This, however, is beyond the scope of the present article.

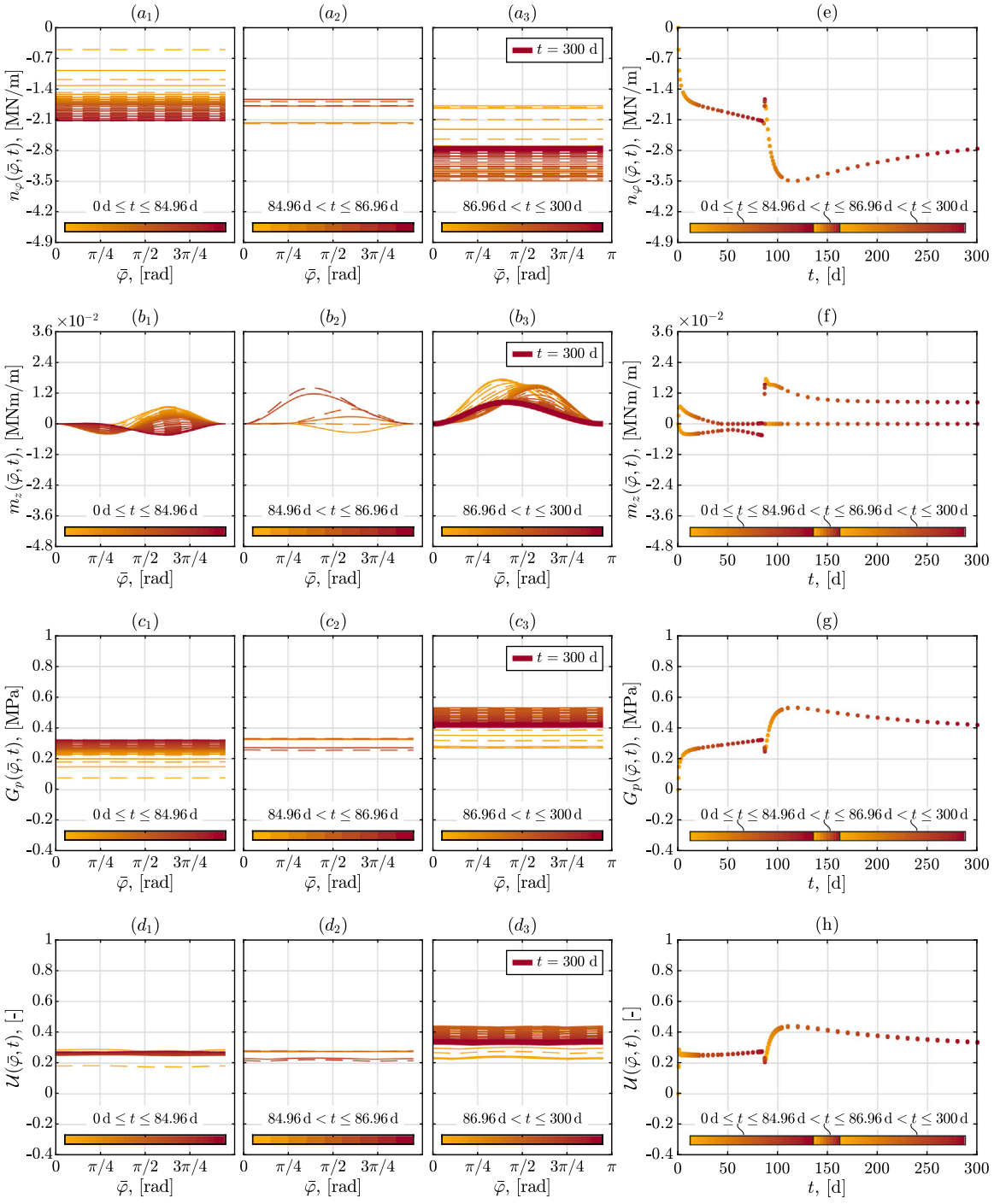

Fig. 21. Distribution of circumferential normal forces (a), bending moments (b), ground pressure (c), and degree of utilization (d) along the circumference of the top heading and associated with construction phases CP1, CP2, and CP3 (index 1-3) of tunnel Stein at measurement cross section KMA5.3.000201, and the temporal evolution of maximum and minimum values (e-h); computed from displacement measurements at MP1, MP4, and MP5 only.

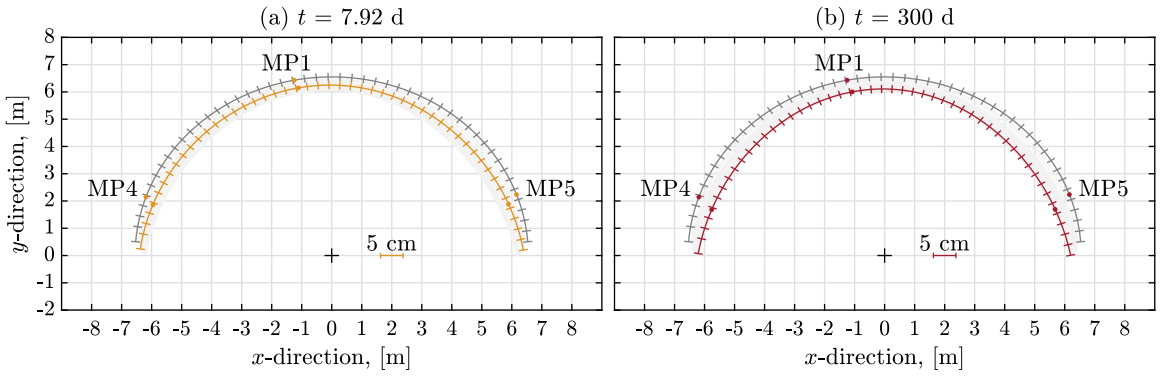

Fig. 22. Midsurface displacement distribution with corresponding shell generator lines of length h = 0.30 m at two different time instants t, at the measurement cross-section KMA5.3.000201 of tunnel Stein, on the basis of measurement data collected from MP1, MP4, and MP5 only (magnification factor of the displacements: 15).

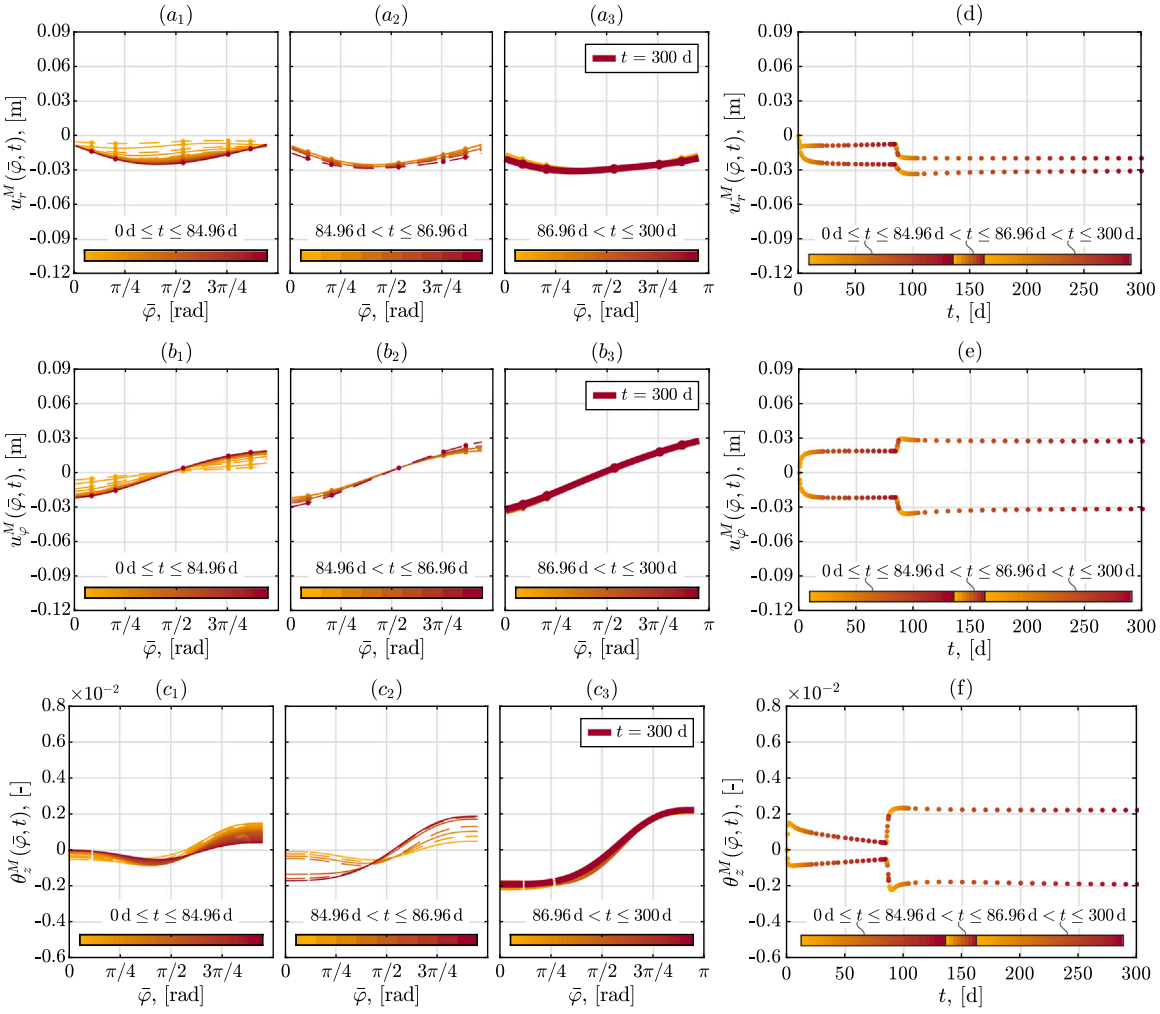

Fig. 23. Distribution of radial and circumferential displacements (a-b), and generator rotations (c) along the circumference of the top heading and associated with construction phases CP1, CP2, and CP3 (index 1-3) of tunnel Stein at measurement cross section KMA5.3.000201, and the temporal evolution of maximum and minimum values (d-f); computed from displacement measurements at MP1, MP4, and MP5 only.

CRediT authorship contribution statement

Raphael Scharf: Writing – original draft, Validation, Software, Methodology, Investigation. **Markus Brandtner:** Writing – review & editing, Resources, Data curation. **Bernd Moritz:** Writing – review & editing, Resources, Funding acquisition, Data curation. **Bernhard Pichler:** Writing – review & editing, Methodology, Funding acquisition, Formal analysis, Conceptualization. **Christian Hellmich:** Writing – review & editing, Writing – original draft, Supervision, Project administration, Methodology, Funding acquisition, Formal analysis, Conceptualization.

Declaration of competing interest

The authors declare that they have no known competing financial interests or personal relationships that could have appeared to influence the work reported in this paper.

Table 7
Displacement measurements from geodetic reflectors, in terms of polar displacement components u_r^{MPi}, u_φ^{MPi} (in meters) associated with measurement points MP1 to MP5, installed at cross section KMA5.3.000201 of tunnel Stein (part 1/2); as seen in Fig. 3.

Viewing time	u_r^{MP1}	u_φ^{MP1}	u_r^{MP2}	u_φ^{MP2}	u_r^{MP3}	u_φ^{MP3}	u_r^{MP4}	u_φ^{MP4}	u_r^{MP5}	u_φ^{MP5}
0.00 d	±0.00000	±0.00000	±0.00000	±0.00000	±0.00000	±0.00000	±0.00000	±0.00000	±0.00000	±0.00000
0.92 d	−0.00744	+0.00206	−0.00555	+0.00554	−0.01229	−0.00171	−0.00760	+0.00636	−0.00907	−0.00682
1.96 d	−0.01147	+0.00335	−0.00915	+0.00931	−0.01745	−0.00517	−0.00892	+0.01078	−0.01233	−0.01202
3.04 d	−0.01518	+0.00417	−0.01037	+0.01128	−0.01968	−0.00680	−0.01094	+0.01357	−0.01310	−0.01589
5.04 d	−0.01673	+0.00406	−0.01089	+0.01254	−0.01993	−0.00844	−0.01089	+0.01496	−0.01288	−0.01735
5.92 d	−0.01802	+0.00370	−0.01187	+0.01264	−0.02098	−0.00872	−0.01130	+0.01461	−0.01348	−0.01724
6.96 d	−0.01953	+0.00277	−0.01132	+0.01244	−0.02151	−0.00918	−0.01274	+0.01633	−0.01422	−0.01899
7.92 d	−0.01818	+0.00394	−0.01193	+0.01350	−0.02075	−0.00892	−0.01128	+0.01546	−0.01303	−0.01804
8.96 d	−0.01963	+0.00381	−0.01233	+0.01304	−0.02111	−0.00887	−0.01157	+0.01568	−0.01327	−0.01870
9.92 d	−0.02089	+0.00416	−0.01414	+0.01479	−0.02198	−0.01077	−0.01253	+0.01662	−0.01372	−0.02024
10.92 d	−0.01895	+0.00470	−0.01360	+0.01381	−0.02099	−0.00965	−0.01184	+0.01495	−0.01417	−0.01826
12.21 d	−0.02003	+0.00440	−0.01371	+0.01347	−0.02106	−0.00958	−0.01038	+0.01471	−0.01266	−0.01615
13.00 d	−0.01991	+0.00499	−0.01250	+0.01484	−0.02204	−0.00872	−0.01091	+0.01622	−0.01405	−0.01735
13.92 d	−0.02087	+0.00425	−0.01317	+0.01455	−0.02132	−0.01002	−0.01173	+0.01647	−0.01294	−0.01839
14.88 d	−0.02097	+0.00376	−0.01381	+0.01454	−0.02150	−0.00947	−0.01195	+0.01862	−0.01416	−0.02146
16.08 d	−0.02067	+0.00371	−0.01399	+0.01414	−0.02142	−0.01060	−0.01161	+0.01704	−0.01350	−0.01936
16.92 d	−0.02054	+0.00388	−0.01420	+0.01423	−0.02141	−0.01074	−0.01159	+0.01758	−0.01387	−0.02008
18.00 d	−0.02079	+0.00363	−0.01454	+0.01433	−0.02148	−0.01081	−0.01136	+0.01723	−0.01408	−0.01947
19.04 d	−0.02173	+0.00299	−0.01585	+0.01404	−0.02171	−0.01168	−0.01184	+0.01738	−0.01340	−0.02025
19.96 d	−0.02160	+0.00419	−0.01478	+0.01478	−0.02252	−0.01123	−0.01143	+0.01774	−0.01359	−0.02018
21.04 d	−0.02190	+0.00313	−0.01548	+0.01421	−0.02275	−0.01302	−0.01190	+0.01757	−0.01215	−0.01942
22.00 d	−0.02242	+0.00415	−0.01513	+0.01489	−0.02226	−0.01079	−0.01108	+0.01733	−0.01413	−0.02020
22.96 d	−0.02271	+0.00370	−0.01538	+0.01520	−0.02290	−0.01182	−0.01140	+0.01764	−0.01392	−0.02080
38.96 d	−0.02226	+0.00391	−0.01522	+0.01469	−0.02271	−0.01040	−0.01127	+0.01726	−0.01373	−0.01970
40.08 d	−0.02199	+0.00376	−0.01408	+0.01471	−0.02223	−0.01015	−0.01109	+0.01796	−0.01504	−0.02008
41.00 d	−0.02202	+0.00305	−0.01456	+0.01483	−0.02137	−0.01038	−0.01219	+0.01779	−0.01400	−0.02014
41.96 d	−0.02159	+0.00368	−0.01522	+0.01533	−0.02271	−0.01040	−0.01229	+0.01776		
42.92 d	−0.02227	+0.00442	−0.01447	+0.01440			−0.01144	+0.01805	−0.01384	−0.02030
44.00 d	−0.02386	+0.00514	−0.01583	+0.01702			−0.01137	+0.01543		
45.04 d	−0.02222	+0.00411	−0.01363	+0.01495	−0.02313	−0.01056	−0.01190	+0.01726	−0.01390	−0.02017
45.96 d	−0.02252	+0.00366	−0.01472	+0.01535	−0.02188	−0.01126	−0.01168	+0.01754	−0.01407	−0.02032
47.96 d	−0.02389	+0.00392	−0.01617	+0.01585	−0.02279	−0.01139			−0.01464	−0.02043
54.96 d	−0.02281	+0.00371	−0.01496	+0.01516	−0.02253	−0.01109	−0.01187	+0.01779	−0.01343	−0.02034
66.04 d	−0.02271	+0.00420	−0.01527	+0.01554	−0.02275	−0.01089	−0.01150	+0.01793	−0.01368	−0.02014
72.96 d	−0.02460	+0.00549	−0.01552	+0.01663	−0.02385	−0.01033	−0.01140	+0.01733	−0.01374	−0.02002
76.96 d			−0.01479	+0.01606	−0.02156	−0.00954	−0.01172	+0.01827	−0.01290	−0.02064
79.00 d	−0.02315	+0.00459	−0.01506	+0.01623	−0.02333	−0.01065	−0.01130	+0.01767	−0.01361	−0.01996
81.08 d	−0.02356	+0.00508	−0.01461	+0.01647	−0.02383	−0.01061	−0.01093	+0.01812	−0.01465	−0.01958
81.96 d	−0.02470	+0.00551	−0.01564	+0.01679	−0.02270	−0.01054				
82.96 d	−0.02246	+0.00497	−0.01473	+0.01599	−0.02303	−0.01091	−0.01134	+0.01840	−0.01431	−0.02013
83.96 d	−0.02265	+0.00348	−0.01593	+0.01604	−0.02428	−0.01021	−0.01194	+0.01798	−0.01349	−0.01990
84.96 d	−0.02477	+0.00308	−0.01740	+0.01626	−0.02433	−0.01284	−0.01229	+0.01839	−0.01483	−0.02154
85.96 d	−0.02630	+0.00409	−0.01818	+0.01847	−0.02556	−0.01455	−0.01536	+0.02145	−0.01698	−0.02426
86.96 d	−0.02825	+0.00508	−0.02016	+0.01995	−0.02803	−0.01478	−0.01970	+0.02482	−0.02100	−0.02653
88.00 d	−0.02943	+0.00530	−0.02127	+0.02020	−0.02956	−0.01622	−0.02164	+0.02521	−0.02394	−0.02908
89.04 d	−0.02905	+0.00513	−0.02228	+0.02080	−0.03065	−0.01580	−0.02061	+0.02620	−0.02439	−0.02945
89.96 d	−0.02815	+0.00455	−0.02142	+0.02086	−0.03038	−0.01670	−0.02295	+0.02624	−0.02571	−0.03014
91.04 d	−0.03010	+0.00554	−0.02214	+0.02079	−0.03027	−0.01733	−0.02193	+0.02574	−0.02513	−0.03206
91.96 d	−0.02950	+0.00338	−0.02205	+0.02021	−0.02995	−0.01788	−0.02182	+0.02695	−0.02409	−0.03126
93.08 d	−0.03081	+0.00343	−0.02284	+0.02086	−0.03138	−0.01875	−0.02236	+0.02760	−0.02409	−0.03126
93.96 d	−0.02899	+0.00389			−0.03132	−0.01747	−0.02317	+0.02658	−0.02490	−0.03320

Acknowledgments

The authors gratefully acknowledge project FFG-COMET #882504 “Rail4Future: Resilient Digital Railway Systems to enhance performance”. They also acknowledge TU Wien Bibliothek for financial support through its Open Access Funding Programme.

Appendix A. Displacement measurements performed at KMA5.3.000201 of tunnel Stein

Displacements obtained from geodetic reflectors installed at five measurement points were recorded in Cartesian components, u_x^{MPi} and u_y^{MPi}, and transformed to polar components, u_r^{MPi} and u_φ^{MPi}, with $i = 1, 2, 3, 4, 5$, as given in Tables 7 and 8. These polar displacements entered the fitting functions defined through Eqs. (1)–(2).

Appendix B. Force-to-force influence functions

The mathematical expressions for the (external)-traction-to-internal-force influence functions $\mathcal{I}_{N\to f}$ and $\mathcal{I}_{i\to f}$, occurring in Eqs. (10) and (11), read as

$$\mathcal{I}_{N\to f}(\bar{\varphi}) = \cos(\bar{\varphi}) - \frac{\sin(\bar{\varphi})}{\tan(\Delta\varphi)} + \frac{\sin(\bar{\varphi})}{\sin(\Delta\varphi)}\,, \tag{57}$$

$$\mathcal{I}_{i\to f}(\bar{\varphi}) = \left[\cos(\bar{\varphi}) - 1 - \frac{\sin(\bar{\varphi})}{\tan(\Delta\varphi)} + \frac{\sin(\bar{\varphi})}{\sin(\Delta\varphi)}\right] A_i(\bar{\varphi})\,. \tag{58}$$

The derivatives of these functions occur in Eqs. (42) and (43), and the corresponding mathematical expressions read as

$$\frac{\mathrm{d}\mathcal{I}_{N\to f}(\bar{\varphi}=0)}{\mathrm{d}\bar{\varphi}} = \left[-\frac{1}{\tan(\Delta\varphi)} + \frac{1}{\sin(\Delta\varphi)}\right], \tag{59}$$

Table 8
Polar displacement components $u_r^{\mathrm{MP}i}$, $u_\varphi^{\mathrm{MP}i}$ (in meters) measured at geodetic reflectors, the so-called measurement points MP1 to MP5, installed within cross section KMA5.3.000201 of tunnel Stein (part 2/2); as seen in Fig. 3.

Viewing time	u_r^{MP1}	u_φ^{MP1}	u_r^{MP2}	u_φ^{MP2}	u_r^{MP3}	u_φ^{MP3}	u_r^{MP4}	u_φ^{MP4}	u_r^{MP5}	u_φ^{MP5}
94.96 d	−0.03024	+0.00373			−0.03248	−0.01712			−0.02562	−0.03166
96.00 d	−0.02862	+0.00107	−0.02242	+0.01797	−0.02919	−0.01655	−0.02224	+0.02511		
97.13 d	−0.02920	+0.00281	−0.02442	+0.01995			−0.02235	+0.02390	−0.02591	−0.03188
98.00 d	−0.02893	+0.00470	−0.02484	+0.01935			−0.02172	+0.02391		
98.96 d	−0.03003	+0.00379			−0.03172	−0.01353	−0.02055	+0.02389		
99.92 d	−0.03264	+0.00399	−0.02356	+0.02143	−0.03434	−0.01575	−0.02285	+0.02627		
100.96 d	−0.03303	+0.00458	−0.02370	+0.02080	−0.03201	−0.01780	−0.02299	+0.02484		
101.96 d	−0.03039	+0.00610	−0.02154	+0.02179	−0.03344	−0.01548	−0.02135	+0.02499	−0.02814	−0.02980
102.96 d	−0.03002	+0.00593	−0.02199	+0.02013	−0.03319	−0.01490	−0.02140	+0.02423	−0.02863	−0.03174
103.96 d	−0.02982	+0.00436	−0.02248	+0.01947	−0.03002	−0.01689	−0.02320	+0.02329		
127.96 d	−0.02758	+0.00433	−0.02292	+0.01937	−0.02869	−0.01659	−0.02094	+0.02503	−0.02433	−0.02809
128.96 d	−0.02907	+0.00401	−0.02268	+0.01892	−0.02868	−0.01567	−0.02269	+0.02336	−0.02489	−0.02789
129.96 d	−0.02817	+0.00547	−0.02157	+0.01931	−0.03152	−0.01451	−0.02216	+0.02397	−0.02711	−0.02815
130.96 d	−0.02846	+0.00400	−0.02327	+0.01870	−0.02887	−0.01483	−0.02172	+0.02391	−0.02583	−0.02872
132.00 d	−0.03171	+0.00351	−0.02225	+0.01966	−0.03049	−0.01727	−0.02316	+0.02532	−0.02359	−0.02783
132.96 d	−0.03128	+0.00414	−0.02312	+0.01882	−0.03018	−0.01541	−0.02320	+0.02329	−0.02808	−0.03024
134.00 d	−0.02942	+0.00377	−0.02267	+0.01970	−0.03045	−0.01571	−0.02207	+0.02400	−0.02471	−0.02944
138.96 d	−0.02913	+0.00423	−0.02202	+0.02049			−0.02242	+0.02472	−0.02480	−0.03058
140.13 d	−0.03088	+0.00518	−0.02228	+0.02144	−0.03113	−0.01724	−0.02231	+0.02624		
140.96 d	−0.03076	+0.00424	−0.02207	+0.02071	−0.03001	−0.01703	−0.02170	+0.02540	−0.02591	−0.03039
142.04 d	−0.02968	+0.00454	−0.02131	+0.01914	−0.02808	−0.01620	−0.02409	+0.02404	−0.02853	−0.03029
143.04 d	−0.02977	+0.00354	−0.02179	+0.01926	−0.02943	−0.01607	−0.02236	+0.02485	−0.02417	−0.02794
143.96 d	−0.02834	+0.00407	−0.02139	+0.01972	−0.02962	−0.01644	−0.02214	+0.02451	−0.02423	−0.02813
237.33 d	−0.02928	+0.00293	−0.02140	+0.02100	−0.03009	−0.01682	−0.02284	+0.02532	−0.02479	−0.02878

$$\frac{\mathrm{d}\mathcal{I}_{1\to f}(\bar\varphi=0)}{\mathrm{d}\bar\varphi} = \left[-\frac{1}{\tan(\Delta\varphi)}+\frac{1}{\sin(\Delta\varphi)}\right] \times\left[\frac{\bar\varphi_1\big(1-H(-\bar\varphi_1)\big)}{\bar\varphi_1-\bar\varphi_2}+\frac{\bar\varphi_2\big(H(-\bar\varphi_2)-1\big)}{\bar\varphi_1-\bar\varphi_2}\right], \tag{60}$$

$$\frac{\mathrm{d}\mathcal{I}_{i\to f}(\bar\varphi=0)}{\mathrm{d}\bar\varphi} = \left[-\frac{1}{\tan(\Delta\varphi)}+\frac{1}{\sin(\Delta\varphi)}\right] \times\left[\frac{\bar\varphi_i\,(\bar\varphi_{i+1}-\bar\varphi_{i-1})\,H(-\bar\varphi_i)}{(\bar\varphi_{i-1}-\bar\varphi_i)(\bar\varphi_i-\bar\varphi_{i+1})} +\frac{\bar\varphi_{i-1}\,H(-\bar\varphi_{i-1})}{\bar\varphi_{i-1}-\bar\varphi_i}+\frac{\bar\varphi_{i+1}\,H(-\bar\varphi_{i+1})}{\bar\varphi_i-\bar\varphi_{i+1}}\right], \tag{61}$$

with $i=2,\dots,7$,

$$\frac{\mathrm{d}\mathcal{I}_{8\to f}(\bar\varphi=0)}{\mathrm{d}\bar\varphi} = \left[-\frac{1}{\tan(\Delta\varphi)}+\frac{1}{\sin(\Delta\varphi)}\right] \times\left[\frac{\bar\varphi_7\,H(-\bar\varphi_7)}{\bar\varphi_7-\bar\varphi_8}\right], \tag{62}$$

$$\frac{\mathrm{d}\mathcal{I}_{N\to f}(\bar\varphi=\Delta\varphi)}{\mathrm{d}\bar\varphi} = \left[\frac{1}{\tan(\Delta\varphi)}-\frac{1}{\sin(\Delta\varphi)}\right], \tag{63}$$

$$\frac{\mathrm{d}\mathcal{I}_{1\to f}(\bar\varphi=\Delta\varphi)}{\mathrm{d}\bar\varphi} = \left[-\frac{1}{\tan(\Delta\varphi)}+\frac{1}{\sin(\Delta\varphi)}\right] \times\left[\frac{(\bar\varphi_1-\Delta\varphi)\,H(\Delta\varphi-\bar\varphi_1)-\bar\varphi_1}{\bar\varphi_1-\bar\varphi_2} +\frac{\bar\varphi_2+(\Delta\varphi-\bar\varphi_2)\,H(\Delta\varphi-\bar\varphi_2)}{\bar\varphi_1-\bar\varphi_2}\right], \tag{64}$$

$$\frac{\mathrm{d}\mathcal{I}_{i\to f}(\bar\varphi=\Delta\varphi)}{\mathrm{d}\bar\varphi} = \left[-\frac{1}{\tan(\Delta\varphi)}+\frac{1}{\sin(\Delta\varphi)}\right] \times\left[\frac{(\bar\varphi_i-\Delta\varphi)(\bar\varphi_{i-1}-\bar\varphi_{i+1})H(\Delta\varphi-\bar\varphi_i)}{(\bar\varphi_{i-1}-\bar\varphi_i)(\bar\varphi_i-\bar\varphi_{i+1})} +\frac{(\Delta\varphi-\bar\varphi_{i-1})\,H(\Delta\varphi-\bar\varphi_{i-1})}{\bar\varphi_{i-1}-\bar\varphi_i} +\frac{(\Delta\varphi-\bar\varphi_{i+1})\,H(\Delta\varphi-\bar\varphi_{i+1})}{\bar\varphi_i-\bar\varphi_{i+1}}\right], \tag{65}$$

with $i=2,\dots,7$,

$$\frac{\mathrm{d}\mathcal{I}_{8\to f}(\bar\varphi=\Delta\varphi)}{\mathrm{d}\bar\varphi} = \left[-\frac{1}{\tan(\Delta\varphi)}+\frac{1}{\sin(\Delta\varphi)}\right] \times\left[\frac{(\Delta\varphi-\bar\varphi_7)\,H(\Delta\varphi-\bar\varphi_7)}{\bar\varphi_7-\bar\varphi_8}\right]. \tag{66}$$

Data availability

Measurement data given in Tables 7 and 8; analytical formulae given in text.

References

Ausweger, M., Binder, E., Lahayne, O., Reihsner, R., Maier, G., Peyerl, M., Pichler, B., 2019. Early-age evolution of strength, stiffness, and non-aging creep of concretes: Experimental characterization and correlation analysis. Materials 12 (2), 481–489. http://dx.doi.org/10.3390/ma12020207.

Benedikt, J., Wagner, H., Herzeg, T., 2016. The St. Kanzian chain of tunnels – tunnelling under very varied and extremely difficult conditions. Geomech. Tunnel. 9 (5), 405–415. http://dx.doi.org/10.1002/geot.201600044.

Brandtner, M., Moritz, B., Schubert, P., 2007. On the challenge of evaluating stress in a shotcrete lining: Experiences gained in applying the hybrid analysis method. Felsbau 25 (5), 93–98.

CEB-FIB, 2010. Model Code for Concrete Structures 2010. Berlin, Germany, Ernst & Sohn.

Fenner, R., 1938. Untersuchungen zur Erkenntnis des Gebirgsdrucks [Investigations to the Knowledge of the Rock Pressure]. Glückauf, Berg- und Hüttenmännische Zeitschrift 32, 681–695.

Gamnitzer, P., Neuner, M., Schreter-Fleischhacker, M., Dummer, A., Mader, T., Smaniotto, S., Hofstetter, G., 2023. Key features of numerical models for the FE-simulation of deep tunnel advance by the NATM. Undergr. Space http://dx.doi.org/10.1016/j.undsp.2023.06.007.

Germain, P., 1973a. La méthode des puissances virtuelles en mécanique des milieux continus. I: Théorie du second gradient. J. Mécanique 12 (2), 235–274.

Germain, P., 1973b. The method of virtual power in continuum mechanics. Part 2: Microstructure. SIAM J. Appl. Math. 25 (3), 556–575. http://dx.doi.org/10.1137/0125053.

Hellmich, C., Macht, J., Mang, H., 1999a. Ein hybrides Verfahren zur Bestimmung der Auslastung von Spritzbetonschalen [A Hybrid Method for Determination of the Degree of Utilization of Shotcrete Tunnel Shells]. Felsbau 17 (5), 422–425.

Hellmich, C., Mang, H., 2005. Shotcrete elasticity revisited in the framework of continuum micromechanics: From submicron to meter level. J. Mater. Civ. Eng. 17 (3), 246–256. http://dx.doi.org/10.1061/(ASCE)0899-1561(2005)17:3(246).

Hellmich, C., Mang, H., Ulm, F., 2001. Hybrid method for quantification of stress states in shotcrete tunnel shells: combination of 3D in situ displacement measurements and thermochemoplastic material law. Comput. Struct. 79 (22-25), 2103–2115. http://dx.doi.org/10.1016/S0045-7949(01)00057-8.

Hellmich, C., Pichler, B., Heissenberger, R., Moritz, B., 2020. 150 years reliable railway tunnels–extending the hybrid method for the long-term safety assessment. Geomech. Tunnel. 13 (5), 538–546. http://dx.doi.org/10.1002/geot.202000023.

Hellmich, C., Ulm, F.-J., Mang, H.A., 1999b. Multisurface chemoplasticity. I: Material model for shotcrete. J. Eng. Mech. 125 (6), 692–701. http://dx.doi.org/10.1061/(ASCE)0733-9399(1999)125:6(692).

Herzeg, T., Moraus, T., 2017. St. Kanzian tunnel chain – current state of works [Tunnelkette St. Kanzian – Aktueller Stand der Arbeiten]. Geomech. Tunnel. 10 (6), 740–747. http://dx.doi.org/10.1002/geot.201700048.

Höller, R., Aminbaghai, M., Eberhardsteiner, L., Eberhardsteiner, J., Blab, R., Pichler, B., Hellmich, C., 2019. Rigorous amendment of Vlasov's theory for thin elastic plates on elastic Winkler foundations, based on the principle of virtual power. Eur. J. Mech. A Solids 73, 449–482. http://dx.doi.org/10.1016/j.euromechsol.2018.07.013.

Ieronymaki, E., Whittle, A.J., Einstein, H.H., 2018. Comparative study of the effects of three tunneling methods on ground movements in stiff clay. Tunnel. Undergr. Space Technol. 74, 167–177. http://dx.doi.org/10.1016/j.tust.2018.01.005.

Jiang, Z., Liu, X., Mang, H.A., Zhang, J., Pichler, B., 2024. Convergence-related serviceability limit states of segmental tunnel rings: Lessons learned from structural analysis of real-scale tests. Appl. Sci. 14 (13), 5483. http://dx.doi.org/10.3390/app14135483.

Karakuş, M., Fowell, R.J., 2004. An insight into the new Austrian tunnelling method (NATM). In: 7th Regional Rock Mechanics Symposium, Sivas, Turkey.

Königsberger, M., Irfan-ul Hassan, M., Pichler, B., Hellmich, C., 2016. Downscaling based identification of nonaging power-law creep of cement hydrates. J. Eng. Mech. 142 (12), 04016106. http://dx.doi.org/10.1061/(ASCE)EM.1943-7889.0001169.

Kupfer, H., 1973. Das Verhalten Des Betons Unter Mehrachsiger Kurzzeitbelastung Unter Besonderer Berücksichtigung Der Zweiachsigen Beanspruchung [The Behavior of Concrete Under Multiaxial Short Time Loading Especially Considering the Biaxial Stress]. Deutscher Ausschuss für Stahlbeton e. V., Heft 229, Ernst & Sohn.

Niedbalski, Z., Małkowski, P., Majcherczyk, T., 2018. Application of the NATM method in the road tunneling works in difficult geological conditions–The Carpathian flysch. Tunnel. Undergr. Space Technol. 74, 41–59. http://dx.doi.org/10.1016/j.tust.2018.01.003.

ÖGG-Guideline, 2023. Recommendations for the Design of Reinforced Sprayed Concrete Linings Based on EN 1992 and EN 1997. Austrian Society for Geomechanics.

ÖNORM EN 1992-1-1, 2015. Bemessung und konstruktion von stahlbeton- und spannbetontragwerken - teil 1-1: Allgemeine bemessungsregeln und regeln für den hochbau (konsolidierte fassung). Austrian Standars International.

Pacher, F., 1964. Deformationsmessungen im Versuchsstollen als Mittel zur Erforschung des Gebirgsverhaltens und zur Bemessung des Ausbaus [Measurements of Deformations in Experimental Tunnels to explore the Behavior of Rock and to Design the Lining]. Felsmechanik und Ingenieurgeologie 1, 149–695.

Pichler, B., Scheiner, S., Hellmich, C., 2008. From micron-sized needle-shaped hydrates to meter-sized shotcrete tunnel shells: micromechanical upscaling of stiffness and strength of hydrating shotcrete. Acta Geotech. 3, 273–294. http://dx.doi.org/10.1007/s11440-008-0074-z.

Rabcewicz, L.v., 1964a. The new Austrian tunnelling method, part one. Water Power 16, 453–457.

Rabcewicz, L.v., 1964b. The new Austrian tunnelling method, part two. Water Power 16, 511–515.

Rabcewicz, L.v., 1965. The new Austrian tunnelling method, part three. Water Power 17, 19–24.

Ramspacher, V.W., Druckfeuchter, H., 1999. Baulos 3 - Siebergtunnel [Construction lot 3 - Sieberg tunnel] (in German). Felsbau 17 (2), 84–89.

Razgordanisharahi, A., Sorgner, M., Pilgerstorfer, T., Moritz, B., Hellmich, C., Pichler, B.L., 2024. Realistic long-term stress levels in a deep segmented tunnel lining, from hereditary mechanics-informed evaluation of strain measurements. Tunnell. Undergr. Space Technol. 145, 105602. http://dx.doi.org/10.1016/j.tust.2024.105602.

Ruiz, M.F., Muttoni, A., Gambarova, P.G., 2007. Relationship between nonlinear creep and cracking of concrete under uniaxial compression. J. Adv. Concr. Technol. 5 (3), 383–393. http://dx.doi.org/10.3151/jact.5.383.

Scharf, R., Pichler, B., Heissenberger, R., Moritz, B., Hellmich, C., 2022. Data-driven analytical mechanics of aging viscoelastic shotcrete tunnel shells. Acta Mech. 233, 2989–3019. http://dx.doi.org/10.1007/s00707-022-03235-1.

Scharf, R., Sorgner, M., Scheiner, S., Pichler, B., Hellmich, C., 2024. Viscoelasticity of hydrating shotcrete as key to realistic tunnel shell stress assessment with the new Austrian tunneling method. Mech. Adv. Mater. Struct. 1–16. http://dx.doi.org/10.1080/15376494.2024.2332474.

Scheiner, S., Hellmich, C., 2009. Continuum microviscoelasticity model for aging basic creep of early-age concrete. J. Eng. Mech. 135 (4), 307–323. http://dx.doi.org/10.1061/(ASCE)0733-9399(2009)135:4(307).

Schubert, W., Moritz, B., 2011. State of the art in evaluation and interpretation of displacement monitoring data in tunnels/Stand der Auswertung und Interpretation von Verschiebungsmessdaten bei Tunneln. Geomech. Tunnell. 4 (5), 371–380. http://dx.doi.org/10.1002/geot.201100033.

Schubert, W., Steindorfer, A., 1996. Selective displacement monitoring during tunnel excavation. Felsbau 14 (2), 93–97.

Schubert, W., Steindorfer, A., Button, E.A., 2002. Displacement monitoring in tunnels - an overview. Felsbau 20, 7–15.

Soranzo, E., Guardiani, C., Wu, W., 2022. The application of reinforcement learning to NATM tunnel design. Undergr. Space 7 (6), 990–1002. http://dx.doi.org/10.1016/j.undsp.2022.01.005.

Steindorfer, A., Schubert, W., Rabensteiner, K., 1995. Problemorientierte Auswertung geotechnischer Messungen - Neue Hilfsmittel und Anwendungsbeispiele [Advanced Analysis of geotechnical Displacement Monitoring Data: New Tools and Examples of Application]. Felsbau 13 (6), 386–390.

Touratier, M., 1992. A refined theory of laminated shallow shells. Int. J. Solids Struct. 29 (11), 1401–1415. http://dx.doi.org/10.1016/0020-7683(92)90086-9.

Ullah, S., Pichler, B., Hellmich, C., 2013. Modeling ground-shell contact forces in NATM tunneling based on three-dimensional displacement measurements. J. Geotech. Geoenviron. Eng. 139 (3), 444–457. http://dx.doi.org/10.1061/(ASCE)GT.1943-5606.0000791.

Ullah, S., Pichler, B., Scheiner, S., Hellmich, C., 2010. Shell-specific interpolation of measured 3D displacements, for micromechanics-based rapid safety assessment of shotcrete tunnels. Comput. Model. Eng. Sci. 57 (3), 279–316. http://dx.doi.org/10.3970/cmes.2010.057.279.

Ullah, S., Pichler, B., Scheiner, S., Hellmich, C., 2012. Influence of shotcrete composition on load-level estimation in NATM-tunnel shells: Micromechanics-based sensitivity analyses. Int. J. Numer. Anal. Methods Geomech. 36, 1151–1180. http://dx.doi.org/10.1002/nag.1043.

Zhang, J.-L., Vida, C., Yuan, Y., Hellmich, C., Mang, H.A., Pichler, B., 2017. A hybrid analysis method for displacement-monitored segmented circular tunnel rings. Eng. Struct. 148, 839–856. http://dx.doi.org/10.1016/j.engstruct.2017.06.049.